



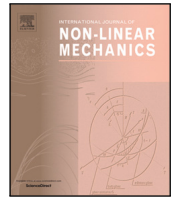
## **Stick–slip oscillations in the low feed linear motion of a grinding machine due to dry friction and backlash**

Downloaded from: <https://research.chalmers.se>, 2024-11-18 23:42 UTC

Citation for the original published paper (version of record):

Iklodi, Z., Piironen, P., Franco, O. et al (2025). Stick–slip oscillations in the low feed linear motion of a grinding machine due to dry friction and backlash. *International Journal of Non-Linear Mechanics*, 168. <http://dx.doi.org/10.1016/j.ijnonlinmec.2024.104940>

N.B. When citing this work, cite the original published paper.



# Stick–slip oscillations in the low feed linear motion of a grinding machine due to dry friction and backlash

Zsolt Iklodi <sup>a,b,\*</sup>, Petri T. Piironen <sup>c</sup>, Oier Franco <sup>d</sup>, Xavier Beudaert <sup>d</sup>, Zoltan Dombovari <sup>a,b</sup>

<sup>a</sup> Department of Applied Mechanics, Faculty of Mechanical Engineering, Budapest University of Technology and Economics, Műgyetem rkp. 3., H-1111 Budapest, Hungary

<sup>b</sup> MTA-BME Lendület Machine Tool Vibration Research Group, Budapest University of Technology and Economics, Budapest H-1521, Hungary

<sup>c</sup> Chalmers University of Technology, Sweden

<sup>d</sup> IDEKO, Dynamics & Control Department, Elgoibar, Basque Country, Spain

## ARTICLE INFO

**Keywords:**  
Grinding  
Stick–slip  
Backlash  
Feed drive  
Control

## ABSTRACT

This paper deals with mechanical modelling and numerical bifurcation analysis of stick–slip oscillations that plague extremely low feed grinding operations. Based on experimental observations, a novel two degree of freedom mechanical model of a grinding machine feed drive system is formulated, which incorporates Stribeck-type dry friction, position and velocity controller dynamics, and actuator backlash. Loss and re-establishment of contact between the feed drive elements is modelled through both rigid-body impacts and a contact-stiffness model. The resulting piecewise-smooth equations of motion are subjected to detailed stability and bifurcation analysis with the help of shooting and collocation based numerical continuation tools. Major focus is attributed to the influence of the feed velocity and the control-loop parameters as well as the identification of stable, stick–slip free parameter regimes. Finally, a controller enhancement strategy is proposed, based on event-driven integrator reset rules, to help limit the amplitude of arising limit-cycle oscillations.

## 1. Introduction

In most engineering applications, state of the art friction compensation techniques [1–3] can effectively stabilize constant-speed machine parts with linear or circular motion. However, there are still critical fields, such as drill-string operations [4] and nano-positioning stages [5], where stick–slip oscillations cause major difficulties. One such case is high-precision grinding, where extremely low feed rates, often as low as 10–100  $\mu\text{m}/\text{min}$ , must be used for reaching the expected surface roughness, integrity, and accuracy requirements. Preventing the emergence of stick–slip oscillations is essential when operating grinding processes, as a non-constant feed rate can lead to subpar surface quality and undesirable cutting-mark patterns that are visible to the naked eye [6,7].

Moving the grinding wheel in a smooth and even manner at low feed rates is especially challenging in the presence of dry friction. It has been observed experimentally [8] that even if a well-tuned velocity and position control system is employed, the Stribeck effect may cause the desired constant speed motion to become unstable, and be replaced by emerging stick–slip oscillations, often referred to as hunting oscillations [9,10]. The control task is only further hindered by the backlash inherently present in the geared drive systems commonly

used for providing the feed motion of CNC machines [11,12]. Here, the effect is also of a similar order of magnitude as the tolerances prescribed for the grinding operation. This backlash can considerably increase the amplitude of limit-cycle oscillations if they also contain segments of contact loss. Furthermore, at velocity reversal events in bistable parameter regimes, backlash can also induce sudden jumps from the desired stable steady-state solution to undesirable limit cycles.

If stick–slip oscillations are encountered when a grinding machine is trying to create a steady feed motion, the desired uniformly and linearly increasing position signal of the grinding wheel will be replaced by a step-wise uneven motion. As these steps leave noticeable marks on the machined workpiece, it is of great industrial importance, to accurately model the phenomena which lead to the emergence of these harmful hunting motions. Empirical evidence suggests, that the root cause of this problem is the intricate interplay of the dry-friction and backlash present in the feed drive assembly of the grinding machine. As of yet, there are no sufficiently detailed analytic or numeric studies, which account for both of these non-smooth effects. The main aim of this paper is to fill this research gap.

The combined effect of dry friction and backlash, although scarcely researched, has shown to result in intricate dynamic behaviours [13,14]

\* Corresponding author.

E-mail addresses: [zsolt.iklodi@mm.bme.hu](mailto:zsolt.iklodi@mm.bme.hu) (Z. Iklodi), [dombovari@mm.bme.hu](mailto:dombovari@mm.bme.hu) (Z. Dombovari).

and major control challenges [15,16]. This paper formulates a low-dimensional mechanical model of the feed drive assembly of a grinding machine, which incorporates both of these nonlinear effects, in order to help us to better understand the emergence of stick–slip oscillations, and to facilitate their prevention. This model is used to conduct a detailed numerical bifurcation analysis of the system to identify the effects of the feed velocity and controller parameters. Based on these results, safe parameter regimes are identified and a control strategy for stick–slip prevention is proposed.

Here, the feed drive assembly is modelled as a two degree of freedom (DoF) lumped mass model based on modal characterization of the grinding machine [17,18]. Backlash is taken into account as a clearance and a conditional contact between these two masses, with both a compliant contact stiffness and a fully rigid impact model implemented for the description of the contact dynamics [19–21]. Based on experimental data available on dry friction in machine tool feed drives [22–25] a Stribeck-type force characteristic is considered. Finally, the constant feed motion is enforced by an industry standard cascaded proportional position (P) and proportional–integral (PI) velocity control architecture [26–28].

Due to the non-smooth nature of both the considered friction force and the backlash, this system is governed by a set of piecewise-smooth ordinary differential equations (PWS-ODEs). In the past few decades these types of systems have received ample scientific attention [29–31], and various aspects of their dynamics have been thoroughly examined. Nevertheless, due to their highly intricate dynamic behaviour and high parameter sensitivity, the in-depth analytical and numerical analysis of such systems, e.g. with dry friction [32] and/or backlash [33], still remains a significant challenge. During parameter variation, abrupt changes in a solution branch caused by a discontinuity-induced bifurcation, such as grazing [34], sliding [35] or even chatter [36], and the resulting changes in its solution signature, makes uncovering detailed bifurcation diagrams very tedious. To make matters even worse, with the introduction of each new distinct non-smooth effect the level of complexity in these systems grows exponentially [37].

This explosion of complexity is demonstrated well by Yadav et al. [14] who studied a Centre Buffer Coupler model, with both dry friction and backlash. They identified nine distinct subspaces with different dynamic behaviours, connected by a set of four intersecting event surfaces and a large set of distinguishable non-smooth events. In the feed drive assembly of the grinding model discussed in the present paper, the topology of the state space is very similar, yet, the models differ in several aspects. The system discussed here has two degrees of freedom, and incorporates more nuanced friction and contact models. The inclusion of the Stribeck effect is necessary to explain how the stability of the uniform feed rate motion can be lost, while the more elaborate contact models are crucial for circumventing unrealistic cases where the linear contact force would become negative at the point of separation due to the inclusion of a viscous damping term. To avoid having to deal with multiple switching surfaces for contact loss events, here, when contact is modelled as compliant, a Kelvin–Voigt type nonlinear force is considered. Furthermore, compared to [14] and other studies concerning both dry friction and backlash [13,16], the numerical analysis presented in this paper also goes beyond time-domain simulations by employing continuation of periodic orbits, in order to provide a more in-depth look into the non-smooth dynamics of the system.

Numerical continuation tools, based on shooting [38] and collocation [39,40], are readily available for bifurcation analysis of periodic orbits in piecewise-smooth systems. Nevertheless, to allow greater freedom when it comes to numerics, in this paper, problem-specific schemes have been implemented. First, a simulation framework with automatic event detection and mode transition handling has been developed to allow a blind search for stable periodic orbits. Then, through the extension of this simulation framework a shooting method with automatic solution signature updates has been formulated. Finally,

a piecewise-Chebyshev polynomial based collocation framework has been employed, to considerably improve the speed of numeric continuation and allow a more robust handling of grazing and sliding bifurcations. The combined use of these numerical tools allowed for an efficient formulation of bifurcation diagrams and an in-depth analysis of the effect of system parameters.

To help improve the dynamic behaviour of the grinding mechanism's feed drive assembly, by limiting the amplitude and period length of the arising stick–slip oscillations, this study proposes an integrator reset rule for controller enhancement. This scheme has been heavily inspired by the hybrid automata controller solution proposed in [41] for the prevention of hunting motions in setpoint control applications with Stribeck-type friction. Compared to the positioning task presented in that paper, here the control goal is slightly different. Ensuring a constant speed, linear motion requires the controller force to offset the unknown sliding friction forces at the desired equilibrium point. In this case, the integrator cannot simply be reset to zero, instead it should be manipulated to a predefined value, which can help the linear guides escape sticking as quickly as possible. Unfortunately this requires a priori knowledge of the maximal static friction force, however, the strategy is still straightforward and simple to implement, and requires no further parameter tuning. Furthermore, to determine the static friction is a lot easier than uncovering the velocity-dependent sliding friction force characteristics, which would be necessary for more elaborate dry-friction compensation solutions [42].

The remainder of this article is structured as follows. Section 2 details the formulation of the low dimensional piecewise-smooth mechanical model of the feed drive assembly for a grinding machine. Section 3 discusses the numerical methods used for the bifurcation analysis of this system, with a major focus on the advantages and disadvantages of each implemented technique. Section 4 presents bifurcation diagrams and details the proposed intervention strategy for the amplitude limitation of stick–slip oscillations. Finally, Section 5 gives concluding remarks.

## 2. Modelling

Even with state of the art instruments, ensuring the even and smooth motion of machine tools on feed rates below 1 mm/min remains a significant engineering and control challenge. As illustrated by Fig. 1, due to the intricate interplay of friction and actuator forces, such systems are highly prone to stick–slip oscillations and may exhibit complicated hunting motions. This phenomenon is clearly demonstrated by the motor and linear encoder position signals shown in Figs. 1(b) and (c). These have been obtained from measurements conducted on a real grinding machine shown in Fig. 1(a). In this machine tool, as illustrated by Fig. 2, the feed motion in the indicated  $x$  direction is provided by a rotary motor through a ball-screw drive, while the moving column carrying the grinding wheel is supported by linear guides. In these guides, the presence of considerable dry-friction and sticktion is clearly indicated by the step-wise nature of the measured position signals. Closer examination of Fig. 1(b) at preprogrammed velocity-reversal events also reveals the presence of clear and significant backlash. This most likely originates from the ball-screw drive [43]. In Fig. 1(c) a complicated hunting behaviour can be seen, which may have been induced by a combined effect of dry-friction and backlash.

The main goal of this paper is to present the simplest possible mechanical model, which can explain how the hunting behaviour captured by the signals shown in Figs. 1(b) and (c), can emerge from extremely low-velocity machine-tool feed motions. Here, to properly capture the effects of backlash, at least two degrees of freedom had to be considered. The first for the moving column (or load) and the second for the motor of the grinding machine. These two DoFs are displayed with different shades of grey on the schematic of the feed drive assembly shown in Fig. 2. It is reasonable to assume that dry friction acts primarily on the first DoF, while the controller forces act

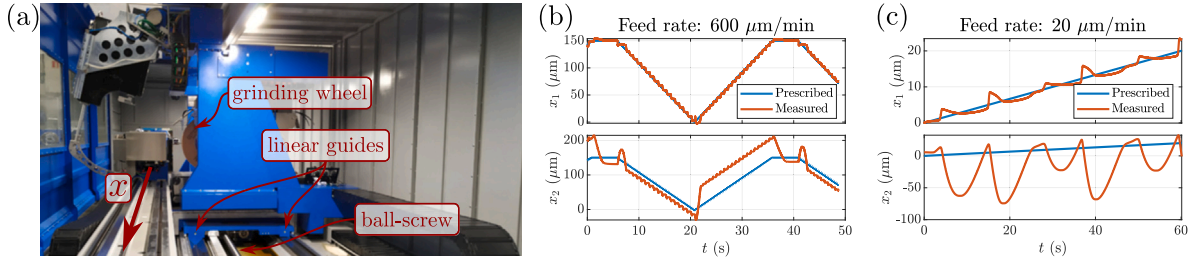


Fig. 1. Hunting motion observed during extreme low feed rate operation of grinding machines. In panels (b) and (c)  $x_1$  and  $x_2$  refer to linear encoder and motor positions, respectively.

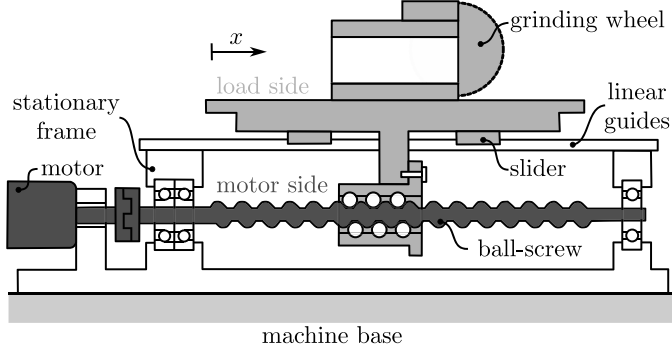


Fig. 2. Schematic of the grinding machine feed drive assembly from Fig. 1.

on the second one. Since the control objective is the accurate reference tracking of the grinding wheel and thus the moving column, this leads to a non-collocated control architecture.

Considering these two degrees of freedom, and modelling them as the lumped masses, results the simplified mechanical model show in Fig. 3(a). Here the movements of the machine tool are defined in a reference frame, which moves with the prescribed feed motion of the grinding wheel. The corresponding feed velocity is marked with  $v_f$ , meaning  $x_{ref} \sim v_f t$ . The relative positions and velocities  $x_1$  and  $x_2$ , as well as  $\dot{x}_1$  and  $\dot{x}_2$  are associated with the machine tool's moving column and motor, respectively. The corresponding modal masses are marked with  $m_1$  and  $m_2$ , while the contact between these two bodies is modelled with a backlash element, which has a dead-zone of size  $2d$ .

The controller force  $F_c$  is provided by the industry standard cascaded P-PI velocity-position control loop presented in Fig. 3(b). Here in accordance with the control goal, both velocity and position feedback relies on signals measured directly on the load side ( $x_1$  and  $\dot{x}_1$ ). It must be noted that in industrial machine tools, velocity measurements on the load side, obtained e.g. via approximate differentiation of the linear encoder position signal, can be too noisy for precise motion control applications, such as providing a uniform low feed rate for grinding operations. Consequently, it may also be worthwhile to analyse the system presented in Fig. 3 while considering velocity feedback on the motor side, thus replacing  $\dot{x}_1$  with  $\dot{x}_2$  in the control loop.

The belt shown in Fig. 3(a) is meant to illustrate that in the previously defined moving reference frame  $x_{ref}$  the machine bed moves with  $-v_f$  relative to the moving column and the grinding wheel. In this relative frame of reference, the friction present in the linear guides is best characterized via the asymmetric Stribeck type curve illustrated in Fig. 3(c). This piecewise nonlinear definition of the friction force  $F_f$  relies on  $\mu$  and  $\mu_0$ , which are the sliding and sticking friction coefficients, as well as the load  $F_n = m_1 g$ , which is the normal force exerted by the moving column on the linear guides of the machine.

As illustrated by Fig. 3(d) the governing equation of motion of the proposed mechanical model takes the form

$$m_1 \ddot{x}_1 = -F_f + F_d, \quad (1a)$$

$$m_2 \ddot{x}_2 = -F_d + F_c, \quad (1b)$$

where  $\ddot{x}_1$  and  $\ddot{x}_2$  refer to the acceleration of the machine tool's moving column and motor, respectively. After unfolding the control loop seen in Fig. 3(b), the controller force can be evaluated as

$$F_c = -K_v \left( \left( K_p + \frac{1}{T_i} \right) x_1 + \dot{x}_1 + \frac{K_p}{T_i} \int_0^t x_1(s) ds \right), \quad (2)$$

while using the characteristics presented in Fig. 3(c) the friction force is described as

$$F_f = \begin{cases} m_1 g \left( \mu + (\mu_0 - \mu) \exp \left( \left( \frac{-\dot{x}_1 + v_f}{v_s} \right)^\delta \right) \right) + b_f (\dot{x}_1 + v_f) & | \dot{x}_1 > -v_f, \\ -m_1 g \left( \mu + (\mu_0 - \mu) \exp \left( \left( \frac{\dot{x}_1 + v_f}{v_s} \right)^\delta \right) \right) + b_f (\dot{x}_1 + v_f) & | \dot{x}_1 < -v_f, \\ [-\mu_0 m_1 g, \mu_0 m_1 g] & | \dot{x}_1 = -v_f. \end{cases} \quad (3)$$

Here the last row is meant to represent that  $F_f$  can take on any value between  $-\mu_0 m_1 g$  and  $\mu_0 m_1 g$  if  $\dot{x}_1 + v_f = 0$ . Due to the relatively long timescale and period length  $T$  of the expected stick-slip oscillations ( $T > 1$  s) compared to the feedback delays  $\tau$  customarily present in CNC position controllers ( $\tau \approx 2 - 4$  ms), the time delay of the control loop is neglected in (2). In Eq. (3), the Stribeck effect is characterized by the velocity  $v_s$  and the exponent  $\delta$ , while  $b_f$  is a linear viscous friction term.

To model the contact dynamics in the backlash element seen in Fig. 3(a) and to evaluate  $F_d$  from (1), as illustrated in Fig. 4, two different approaches are proposed. The first one, seen Fig. 3(a), considers a compliant contact between the two bodies (allowing  $|x_2 - x_1| > d$ ), which is characterized by the contact stiffness  $k_c$ . Here, the energy dissipated during collisions is considered through the introduction of a viscous damping term  $b_c$ . To avoid having non-zero forces at the point of separation, which would lead to significant numerical difficulties during the bifurcation analysis of the system, a Kelvin-Voigt type contact model has been considered [21]. This means that the damping term becomes nonlinear and the contact force is given by

$$F_{d,KV} = \begin{cases} \phi_{d,KV}^+ & | x_2 - x_1 > d \wedge \phi_{d,KV}^+ > 0, \\ \phi_{d,KV}^- & | x_1 - x_2 > d \wedge \phi_{d,KV}^- < 0, \\ 0 & | \text{otherwise,} \end{cases} \quad (4)$$

$$\phi_{d,KV}^+ = k_c (x_2 - x_1 - d) (1 + b_c (\dot{x}_2 - \dot{x}_1)),$$

$$\phi_{d,KV}^- = k_c (x_2 - x_1 + d) (1 - b_c (\dot{x}_2 - \dot{x}_1)).$$

In Fig. 3(b) the contact surfaces are assumed to be completely rigid (only allowing  $|x_2 - x_1| \leq d$ ). Here, while the moving column and the motor are in contact, the purpose of the contact force is to ensure that  $|x_2 - x_1| = d$ , which in turn also guarantees  $\dot{x}_1 = \dot{x}_2$ . Thus, by rearranging (1), this contact force can be expressed as

$$F_{d,RI} = \begin{cases} \phi_{d,RI} & | x_2 - x_1 = d \wedge \phi_{d,RI} > 0, \\ \phi_{d,RI} & | x_1 - x_2 = d \wedge \phi_{d,RI} < 0, \\ 0 & | \text{otherwise,} \end{cases} \quad (5)$$

$$\phi_{d,RI} = \frac{m_1 F_c + m_2 F_f}{m_2 + m_1}.$$

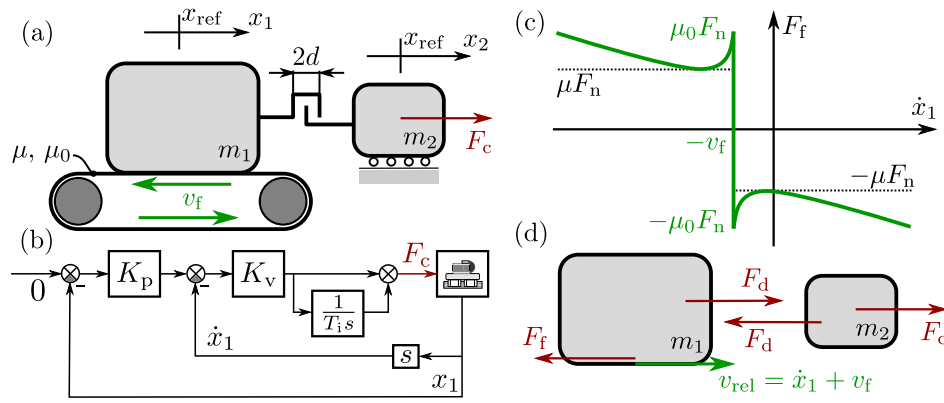


Fig. 3. Simplified mechanical model of a feed drive assembly for a grinding machine.

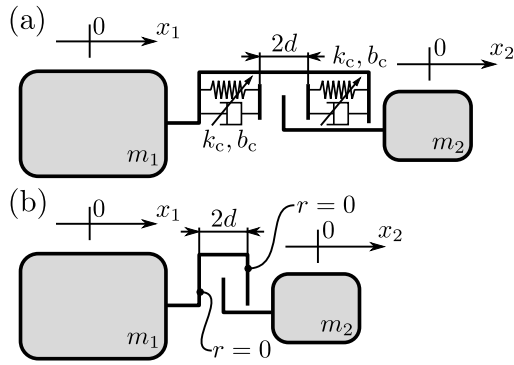


Fig. 4. Contact dynamics models considered in the backlash element between the moving column and motor of the machine tool. Panel (a) shows the Kelvin-Voigt element (KV) and panel (b) the rigid impact model (RI).

For this rigid contact model, the surplus kinetic energy of the two bodies must be dissipated at the instant when contact is established. To avoid having to deal with chatter sequences [36], for this purpose, perfectly inelastic impacts have been considered, with coefficients of restitution  $r = 0$ . This leads to the impact map

$$\dot{x}_1^+ = \dot{x}_2^+ = \frac{m_1 \dot{x}_1^- + m_2 \dot{x}_2^-}{m_1 + m_2}, \quad (6)$$

where the superscripts  $+$  and  $-$ , respectively, refer to the post- and pre-impact states of the system.

Both of the aforementioned contact models have upsides and downsides when it comes to accuracy and ease of numerical treatment. On closer examination of the time signals in Fig. 1, using the Kelvin-Voigt (KV) model appears to be closer to reality since the difference between  $x_1$  and  $x_2$  is clearly not constant while in contact. This model, however, requires the introduction of two difficult-to-measure and highly uncertain parameters  $k_c$  and  $b_c$ . Furthermore, the drastically different timescales of the contact dynamics and the stick-slip oscillations can easily lead to major numerical difficulties.

The rigid impact (RI) model does not require the introduction of new parameters and does not suffer from timescale issues. Nevertheless, this approach suffers from its own set of drawbacks and difficulties. The order reduction of the system when contact is established can lead to singularity issues during bifurcation analysis, and the instantaneous velocity jumps induced by (6) may induce undesirable or unrealistic changes in the modes of  $F_d$  and  $F_f$ .

Prior to numerical analysis of the grinding feed drive assembly, it is worthwhile bringing the governing equation of motion (1) to a first-order nondimensional form. Since  $F_c$  in (2) takes  $x_1, \dot{x}_1$  and the integral of  $x_1$  as an input, the evolution of the system is best described by the

five-dimensional state vector  $\mathbf{y} = [\int x_1 dt, x_1, \dot{x}_1, x_2, \dot{x}_2]^T$ . For the sake of nondimensionalisation,  $x_u = d$  is picked as displacement unit, while  $t_u = \frac{d}{v_S}$  is picked as time unit. This helps considerably in simplifying both the contact and friction force formulas in (3)–(5), and lead to the dimensionless equation of motion

$$\begin{bmatrix} \dot{y}_1 \\ \dot{y}_2 \\ \dot{y}_3 \\ \dot{y}_4 \\ \dot{y}_5 \end{bmatrix} = \begin{bmatrix} y_2 \\ y_3 \\ f_d - f_f \\ y_5 \\ \kappa(f_c - f_d) \end{bmatrix}, \quad (7)$$

where  $\kappa = \frac{m_1}{m_2}$  is the mass ratio and the dimensionless forces are given by

$$f_c = -k_i y_1 - k_p y_2 - k_d y_3, \quad (8)$$

with  $k_i = \frac{K_p K_v d^3}{T_i m_1 v_S^2}$ ,  $k_p = \frac{K_v (K_p + 1/T_i) d^2}{m_1 v_S^2}$ ,  $k_d = \frac{K_v d}{m_1 v_S}$ , and

$$f_f = \begin{cases} \phi \left( 1 + (\eta - 1) \exp \left( (-y_3 - v_0)^\delta \right) \right) + \beta(y_3 + v_0) & | \quad y_3 > -v_0, \\ -\phi \left( 1 + (\eta - 1) \exp \left( (-y_3 - v_0)^\delta \right) \right) + \beta(y_3 + v_0) & | \quad y_3 < -v_0, \\ [-\phi\eta, \phi\eta] & | \quad y_3 = -v_0. \end{cases} \quad (9)$$

with  $\phi = \frac{\mu g d}{v_S}$ ,  $\beta_f = \frac{b_f d}{m_1 v_S}$ ,  $\eta = \frac{\mu_0}{\mu}$ , and  $v_0 = \frac{v_f}{v_S}$ . Depending on what contact model is used, the contact force  $f_d$  may either be

$$f_{d,KV} = \begin{cases} \varphi_{d,KV}^+ & | \quad x_2 - x_1 > 1 \wedge \varphi_{d,KV}^+ > 0, \\ \varphi_{d,KV}^- & | \quad x_1 - x_2 > 1 \wedge \varphi_{d,KV}^- < 0, \\ 0 & | \quad \text{otherwise,} \end{cases} \quad (10)$$

$$\varphi_{d,KV}^+ = \alpha_c (y_4 - y_2 - 1) (1 + \beta_c (y_5 - y_3)),$$

$$\varphi_{d,KV}^- = \alpha_c (y_4 - y_2 + 1) (1 - \beta_c (y_5 - y_3)),$$

with  $\alpha_c = \frac{k_c d^2}{m_1 v_S^2}$  and  $\beta_c = \frac{b_c v_S}{d}$ , or

$$f_{d,RI} = \begin{cases} \varphi_{d,RI} & | \quad x_2 - x_1 = 1 \wedge \varphi_{d,RI} > 0, \\ \varphi_{d,RI} & | \quad x_1 - x_2 = 1 \wedge \varphi_{d,RI} < 0, \\ 0 & | \quad \text{otherwise,} \end{cases} \quad \varphi_{d,RI} = \frac{\kappa f_c + f_f}{1 + \kappa}, \quad (11)$$

with the corresponding impact map

$$\mathbf{y}^+ = \mathbf{g}_{RI}(\mathbf{y}) = \begin{bmatrix} y_1^- & y_2^- & \frac{y_3^- + \kappa y_5^-}{1 + \kappa} & y_4^- & \frac{y_5^- + \kappa y_5^-}{1 + \kappa} \end{bmatrix}^T. \quad (12)$$

Considering the different domains of the friction and contact forces from (9), and (10) or (11), the system of PWS-ODEs (7) that governs the dynamics of the grinding feed drive assembly may be in one of nine different modes. These are illustrated in Fig. 5, and the events connecting these modes are listed in Table 1. Here the notations contact $^+$ , contact $^-$ , and no contact distinguish between the different

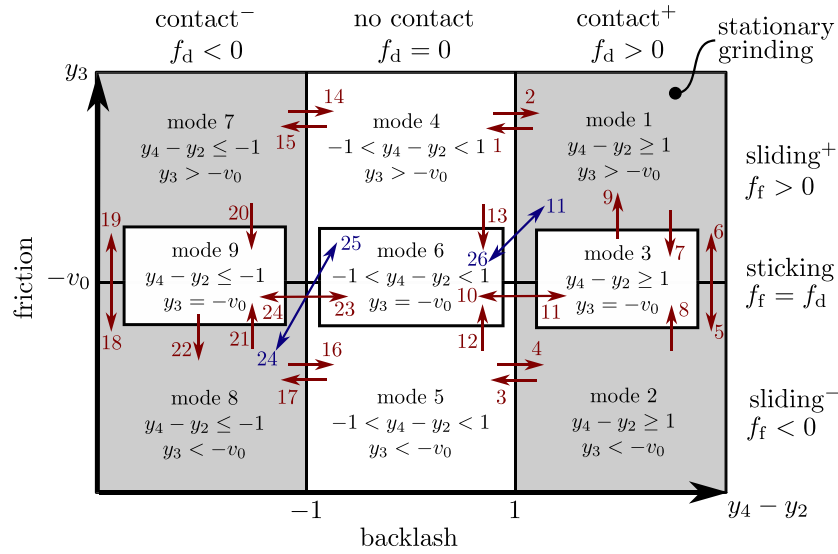


Fig. 5. Mode and event map of the governing system of PWS-ODEs, which takes both dry friction and backlash into account. The mode transitions marked with blue correspond to the rigid impact (RI) contact dynamics model.

domains of the contact force  $f_d$ , while the tags sliding<sup>+</sup>, sliding<sup>-</sup> and sticking mark the different segments of the friction characteristics  $f_f$ .

In an optimal operation the system never leaves mode 1, which means that the contact between the two bodies is uninterrupted and the absolute velocity of the moving column is strictly positive. If the stability of the uniform feed rate solution is lost, growing amplitudes of the limit cycle oscillations may lead to contact loss and velocity reversal events. In case of the former,  $f_d$  becomes zero and the system transitions to mode 4. In case of the latter, when the absolute velocity of the moving column reaches zero there are two things that can happen. If the contact force is greater than the maximal stiction force ( $f_d > \eta\phi$ ) the sliding direction is simply reversed and the system transitions to mode 2. However, if  $f_d \leq \eta\phi$ , the moving column will stick and  $y$  will continue to evolve in mode 3. While the two bodies are in contact, the  $f_d \leq \eta\phi$  condition must be evaluated every time the event condition  $y_3 + v_0 = 0$  is reached, in order to distinguish between the events 5–7, 6–8, 18–20, and 19–21, according to Table 1. From here on, the complexity of the system blows up really quickly, which leads to an intricate web of modes and connecting events. A trajectory may find its way back to mode 1 through the same events playing out in reverse, i.e. establishing contact, separation from sticking, and velocity reversal, or else cover some parts or the entirety of the mode map in Fig. 5.

Upon closer examination of Fig. 5, some mode transitions seem to be missing. First, it is impossible for the moving column not to stick in mode 4 and mode 5, when the event condition  $y_3 + v_0 = 0$  is reached. Second, there is no way to start sliding again from mode 6 without first re-establishing contact. These are both justifiable since in these modes there is no contact between the two bodies and  $f_d = 0$  is guaranteed to be less than the maximal stiction force. Finally, both in positive and negative contact, separation from sticking is only possible in one direction, since in these instances the sign of  $f_d$  is given.

When it comes to the topology of the PWS-ODE mode map in Fig. 5, there are only a few minor differences between the two considered contact models. As marked in brackets in Table 1, all events with event condition  $h_c(\mathbf{y}) = y_4 - y_2 \pm 1 = 0$  are extended with the jump map (12), if the rigid impact (RI) contact model is considered, that is. This induces sudden changes in the velocities of both bodies and can complicate the evaluation of the post-impact sliding direction. Naturally, when leaving mode 6,  $y_3^- = -v_0$  (apart from degenerate cases  $y_5^- \neq y_3^-$ ), which means that the moving column must always start sliding at events 11 and 24. This mode-transition difference is illustrated with blue arrows in Fig. 5. When contact between the two bodies is regained while sliding, the

situation is slightly more complicated. In case of events 2 and 17, the impacts can clearly only push the velocity of the moving column further away from  $-v_0$ , while in case of events 4 and 15, the post-impact sliding direction can be completely arbitrary. At these points,  $\text{sign}(y_3^+ + v_0)$  must be checked on a case-by-case basis to find the post-impact mode of the system. In practice, events 4 and 15 almost never lead to a change in the sliding direction, thus their alternative mode transition directions have been omitted from both Fig. 5 and Table 1.

During numerical continuation of periodic orbits, when using the RI contact model, it has also been observed that when transitioning to sticking from mode 1 or mode 8, there is a possibility for a simultaneous loss of contact if the controller force  $f_c$  and the position difference of the two bodies  $y_4 - y_2$  have opposing signs. Thus, only for the RI contact model, two additional events denoted by the indices 25 and 26 had to be introduced. As seen in Fig. 5, these correspond respectively to the RI model specific mode transitions 24 and 11 playing out in reverse. Comparing Eqs. (10) and (11), it is clear that these two events are exclusive to the RI model. As in the KV case, the sudden change of the friction force  $f_f$ , induced by a transition to sticking, has no immediate effect on the contact force  $f_d$ .

### 3. Numerical methods

As illustrated by the mode map of the PWS-ODE system in Fig. 5 and the corresponding event list in Table 1, the governing equation of motion of the grinding machine feed drive assembly is rich in dynamical complexity and intricacy. Conducting time-domain simulations is the most straightforward approach to get a general sense on its dynamic behaviour, and thus it is an important first step in the numerical analysis. The accurate and reliable time-domain simulation of this system, however, requires great care and effort, e.g. for accurate detection and handling of non-smooth events, or the careful tuning of integration tolerances.

To conduct numerical simulations a MATLAB<sup>®</sup> based framework has been implemented. This made use of the integrator algorithms ode45 and ode15s, as well as their built-in event-detection routines, to find solution trajectories in a segment-by-segment manner. Using a stiff solver such as ode15s proved to be especially rewarding, when the compliant contact model was considered, as it could cope much better with the drastically different timescales of the local and global dynamics. In the implemented framework, at every time instance  $t_j$ ,

**Table 1**

Event definition list for the piecewise-smooth dynamic system from Fig. 5. These events are encountered when  $h_e(\mathbf{y}) = 0$  and the additional inequality conditions found in the cond. column are met. They induce a mode change defined by  $\pi_e$  and a jump in the state according to  $\mathbf{y} \rightarrow \mathbf{g}_e(\mathbf{y})$ , if the rigid body impacts are considered. The output modes displayed in brackets in the  $\pi_e$  column also correspond only to the RI model.

e	Description	$h_e(\mathbf{y})$	Condition	$\pi_e$	$\mathbf{g}_e(\mathbf{y}^-)$
1	contact <sup>+</sup> lost in sliding <sup>+</sup>	$f_d$		1 → 4	
2	contact <sup>+</sup> found in sliding <sup>+</sup>	$y_4 - y_2 - 1$		4 → 1	$\mathbf{g}_{RI}(\mathbf{y}^-)$
3	contact <sup>+</sup> lost in sliding <sup>-</sup>	$f_d$		2 → 5	
4	contact <sup>+</sup> found in sliding <sup>-</sup>	$y_4 - y_2 - 1$		5 → 2	$\mathbf{g}_{RI}(\mathbf{y}^-)$
5	sliding dir. change in contact <sup>+</sup>	$y_3 + v_0$	$f_d > \eta\phi$	1 → 2	
6	sliding dir. change in contact <sup>+</sup>	$y_3 + v_0$	$f_d > \eta\phi$	2 → 1	
7	sticking in contact <sup>+</sup>	$y_3 + v_0$	$f_d \leq \eta\phi$	1 → 3	
8	sticking in contact <sup>+</sup>	$y_3 + v_0$	$f_d \leq \eta\phi$	2 → 3	
9	leaving sticking in contact <sup>+</sup>	$f_d - \eta\phi$		3 → 1	
10	contact <sup>+</sup> lost in sticking	$f_d$		3 → 6	
11	contact <sup>+</sup> found in sticking	$y_4 - y_2 - 1$		6 → 3(1)	$\mathbf{g}_{RI}(\mathbf{y}^-)$
12	sticking without contact	$y_3 + v_0$		4 → 6	
13	sticking without contact	$y_3 + v_0$		5 → 6	
14	contact <sup>-</sup> lost in sliding <sup>+</sup>	$f_d$		7 → 4	
15	contact <sup>-</sup> found in sliding <sup>+</sup>	$y_4 - y_2 + 1$		4 → 7	$\mathbf{g}_{RI}(\mathbf{y}^-)$
16	contact <sup>-</sup> lost in sliding <sup>-</sup>	$f_d$		8 → 5	
17	contact <sup>-</sup> found in sliding <sup>-</sup>	$y_4 - y_2 + 1$		5 → 8	$\mathbf{g}_{RI}(\mathbf{y}^-)$
18	sliding dir. change in contact <sup>-</sup>	$y_3 + v_0$	$f_d > \eta\phi$	7 → 8	
19	sliding dir. change in contact <sup>-</sup>	$y_3 + v_0$	$f_d > \eta\phi$	8 → 7	
20	sticking in contact <sup>-</sup>	$y_3 + v_0$	$f_d \leq \eta\phi$	7 → 9	
21	sticking in contact <sup>-</sup>	$y_3 + v_0$	$f_d \leq \eta\phi$	8 → 9	
22	leaving sticking in contact <sup>-</sup>	$f_d + \eta\phi$		9 → 8	
23	contact <sup>-</sup> lost in sticking	$f_d$		9 → 6	
24	contact <sup>-</sup> found in sticking	$y_4 - y_2 + 1$		6 → 9(8)	$\mathbf{g}_{RI}(\mathbf{y}^-)$
25	contact <sup>-</sup> lost and sticking	$y_3 + v_0$	$f_c > 0$	8 → 6	
26	contact <sup>+</sup> lost and sticking	$y_3 + v_0$	$f_c < 0$	1 → 6	

$j = 1, 2, 3, \dots$  when a zero crossing is detected (see the active event conditions in Table 1), which means that

$$h_{e_j}(\mathbf{y}(t_j)) = 0, \quad (13)$$

the integration of

$$\dot{\mathbf{y}}(t) = \mathbf{f}_{m_j}(\mathbf{y}(t)) \quad (14)$$

is stopped. In this paper, the index  $m_j \in \{1, \dots, 9\}$  is used to distinguish between the possible mode combinations of  $f_f$  and  $f_d$  according to Fig. 5, while  $e_j \in \{1, \dots, 26\}$  is used to enumerate all the possible non-smooth events connecting these modes as seen in Table 1. In (14),  $\mathbf{f}_{m_j}$  represents the active mode of the vector field in (7) during the time interval  $t \in [t_{j-1}, t_j]$ .

At  $t_j$ , the event identifier  $e_j$  marks which event from Table 1 had occurred, and according to which row should the solution be updated. Here, if required the impact map  $\mathbf{y} \rightarrow \mathbf{g}_{RI}(\mathbf{y})$  may be applied and then the integration of (14) can be restarted from  $\mathbf{y}_j^+ = \mathbf{y}^+(t_j)$ , considering the mode of the governing vector field in the subsequent smooth segment  $m_{j+1}$ , which is determined automatically according to  $\pi_{e_j}$ .

This numerical simulation framework allows for quick and easy insights into the dynamic behaviour of the system, and can be employed to identify stable periodic solutions. For a more in-depth numerical analysis of the found periodic orbits, a shooting-method based continuation algorithm is developed. This requires simultaneous solution of the vector field and the first variational equation

$$\dot{\Phi}_j(t) = \partial_{\mathbf{y}} \mathbf{f}_{m_j}(\mathbf{y}(t)) \Phi_j(t), \quad t \in [t_{j-1}, t_j], \quad (15)$$

where  $\Phi_j(t) = \partial_{\mathbf{y}_{j-1}^+} \mathbf{y}(t)$  and  $\Phi_j(t_{j-1}) = \mathbf{I}$ , with  $\mathbf{I}$  denoting a 5 by 5 identity matrix. Following the steps detailed in [39], this allows us to formulate a Jacobian matrix for the boundary value problem

$$\mathbf{y}^+(\mathbf{y}_0^+, t_N) - \mathbf{y}_0^+ = \mathbf{0}, \quad (16)$$

of a nonsmooth periodic orbit with  $N$  events as

$$\mathbf{J}_N = -\mathbf{I} + \prod_{j=N}^1 \partial_{\mathbf{y}} \mathbf{g}_{e_j}(\mathbf{y}_j^-) \mathbf{P}_{e_j} \Phi_j(t_j). \quad (17)$$

Here  $\mathbf{y}_j^-$  refers to the state at  $t_j$  before the jump induced by  $\mathbf{g}_{e_j}$ , and since  $t_j$  is determined via automatic event detection, the necessary corrections at event surface interactions are done according to the derivatives of the projected Poincaré map

$$\mathbf{P}_{e_j} = \mathbf{I} - \frac{\mathbf{f}_{m_j}(\mathbf{y}_j^-) \partial_{\mathbf{y}} h_{e_j}(\mathbf{y}_j^-)}{\partial_{\mathbf{y}} h_{e_j}(\mathbf{y}_j^-) \mathbf{f}_{m_j}(\mathbf{y}_j^-)}. \quad (18)$$

The Jacobian  $\mathbf{J}_N$  from (17) facilitates an efficient solution of (16) via Newton iterations, and enables numeric continuation of even unstable periodic solutions. To do so, a fixed step-size pseudo-arclength method [44] is implemented. Moreover, the simultaneous numerical solution of (15) also allows for stability analysis of located periodic orbits by calculating the Floquet multipliers  $\mu_n = \text{eig}(\Psi_N)$ . This is done through the formulation of the corresponding monodromy matrix

$$\Psi_N = \prod_{j=N}^1 \mathbf{D}_j \Phi_j(t_j), \quad (19)$$

with the necessary saltation matrices available as

$$\mathbf{D}_j = \partial_{\mathbf{y}} \mathbf{g}_{e_j}(\mathbf{y}_j^-) + \frac{(\mathbf{f}_{m_{j+1}}(\mathbf{y}_j^+) - \partial_{\mathbf{y}} \mathbf{g}_{e_j}(\mathbf{y}_j^-) \mathbf{f}_{m_j}(\mathbf{y}_j^-)) \partial_{\mathbf{y}} h_{e_j}(\mathbf{y}_j^-)}{\partial_{\mathbf{y}} h_{e_j}(\mathbf{y}_j^-) \mathbf{f}_{m_j}(\mathbf{y}_j^-)}. \quad (20)$$

Extending the boundary value problem (16) with the additional conditions

$$h_{N,gr} = \partial_{\mathbf{y}} h_{e_N}(\mathbf{y}_N^-) \mathbf{f}_{m_N}(\mathbf{y}_N^-) \quad (21)$$

for grazing and

$$h_{N,sl} = 1 - \left| \frac{\partial_{\mathbf{y}} h_{e_N}(\mathbf{y}_N^-) (\mathbf{f}_{m_1}(\mathbf{y}_1^-) + \mathbf{f}_{m_N}(\mathbf{y}_N^-))}{\partial_{\mathbf{y}} h_{e_N}(\mathbf{y}_N^-) (\mathbf{f}_{m_1}(\mathbf{y}_1^-) - \mathbf{f}_{m_N}(\mathbf{y}_N^-))} \right|, \quad (22)$$

for sliding enables us to continue these critical discontinuity induced bifurcation points in two system parameters. Both conditions are prescribed on the solution  $\mathbf{y}_0$  of (16). Nevertheless, a shooting method, which relies on automatic event detection, is ill-suited for the numeric continuation of grazing bifurcations. The reason is that for slight perturbations of  $\mathbf{y}_0$  the simulated trajectory may not intersect the event

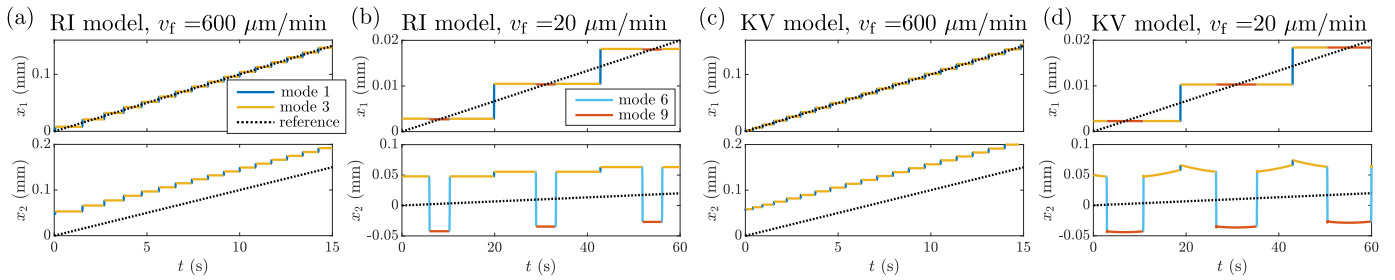


**Fig. 6.** Simulated displacement signals of the grinding feed drive assembly, considering different feed rates and contact models. System parameters are taken from Table 2, while the controller parameters are either  $T_i = 14$  ms,  $K_v = 25$  kNs/m, and  $K_p = 16.667$  1/s for panels (a) and (c), or  $T_i = 16$  ms,  $K_v = 25$  kNs/m, and  $K_p = 16.667$  1/s for panels (b) and (d).

surface it started from, and thus the integration of the governing equation of motion will not stop where it is supposed to. Naturally, this limitation can be circumvented by modifying the algorithms on a case-by-case basis, however, here instead a collocation-based continuation framework has been employed.

Switching over to a multi-segment collocation approach can considerably reduce computation times, make tedious tuning of integration and event detection tolerances unnecessary, and allow for a more robust handling of discontinuity induced bifurcations, e.g. grazing and sliding. Their biggest drawback is their need for *a priori* knowledge of the periodic orbit solution signature. Fortunately, when this sequence of events and modes within a periodic orbit trajectory is already known, thanks to the previously discussed shooting method, and not expected to change on the parameter domain of interest, they can be applied effectively and efficiently. Thus, for the numerical study of the grinding machine feed drive assembly, using shooting and collocation based methods in tandem proved to be the most rewarding approach.

The employed collocation algorithms are discussed in detail in [45]. This paper presents a Chebyshev polynomial based multi-segment spectral collocation [46] framework initially developed for piecewise-smooth delay differential equations. Naturally, it can be used directly for the numeric bifurcation and stability analysis of PWS-ODEs as well. Furthermore, it also enables automatic detection of grazing and sliding bifurcations as well as their continuation in two system parameters. Overall, it provides a reliable alternative for continuing discontinuity induced bifurcations, while its main shortcomings are the establishment of initial solution guesses and branch switching, which can be mitigated efficiently with the help of the shooting method introduced above.

#### 4. Results

The mechanical model of the grinding machine feed drive assembly shown in Fig. 3 has been subjected to a detailed numerical stability and bifurcation analysis to reproduce, explain, and help avoid hunting motions, as illustrated in Figs. 1(b) and (c). This first required the appropriate selection of a base set of system parameters, which is listed in Table 2. Here, the parameters  $\mu$ ,  $\mu_0$ ,  $v_s$ ,  $b_f$ , and  $\delta$  of the Stribeck-type friction model are taken from [25], where the friction-force characterization of the feed drive assembly of a similar CNC machine is presented. The dead zone of the backlash element  $d$  is based on the difference between  $x_1$  and  $x_2$  in Fig. 1(b), while the modal masses  $m_1$  and  $m_2$  were picked to match the timescale of the hunting motion presented in the figure. During this manual parameter fitting of  $m_1$  and  $m_2$ , the rest of the parameters, including  $K_v$ ,  $K_p$ , and  $T_i$  were kept constant on their default values corresponding to the know tuning of the P-PI controller. Finally, the stiffness  $k_c$  of the Kelvin–Voigt contact model was also estimated according to the displacement signals, i.e. on deviations in  $x_2 - x_1$  when the system is in positive contact (mode 1, 2, or 3). The corresponding damping value  $b_c$  was picked so that local contact dynamics would quickly die off,

**Table 2**

The set of base parameters and their dimensions.

Name	Description	Value
$m_1$	modal mass of moving column	146 kg
$m_2$	modal mass of the motor assembly	86 kg
$d$	backlash element dead-zone	45 $\mu$ m
$g$	gravitational acceleration	9.81 m/s <sup>2</sup>
$\mu$	sliding friction coefficient	0.1708
$\mu_0$	sticking friction coefficient	0.3883
$v_s$	Stribeck velocity	6.46 mm/s
$b_f$	viscose friction coefficient	7.27 1/s
$\delta$	Stribeck friction exponent	1
$k_c$	KV contact stiffness	50 kN/mm
$b_c$	KV contact damping term	$1 \times 10^7$ s

**Table 3**

Base dimensionless parameter set corresponding to the values seen in Table 2.

Name	Description	Value
$\kappa$	mass ratio	1.6977
$\phi$	sliding friction magnitude	1.8068
$\eta$	ratio of friction coefficients	2.2734
$\beta$	viscose friction term	$3.4687 \times 10^{-4}$
$\alpha_c$	KV contact stiffness term	16.6179
$\beta_c$	KV contact damping term	477.1195

and to avoid chatter when contact between the two-bodies is established.

Naturally, for an easier treatment of numerical errors and tolerances bifurcation analysis of the system were performed in a nondimensional setting. The equivalent set of dimensionless parameters to the ones in Table 2 is presented in Table 3. The feed rate  $v_f$  and the controller parameters  $T_i$ ,  $K_v$ , and  $K_p$  are not listed in Table 2, as they will be allowed to vary during the stability and bifurcation analysis of the system. Consequently, their dimensionless counterparts  $v_0$ ,  $k_p$ ,  $k_i$ , and  $k_d$  are also omitted from Table 3. The parameter ranges in, which they will be allowed to vary are selected around the default values used for conducting the measurement displayed in Fig. 1(b), meaning  $k_p = 0.732$ ,  $k_d = 1.1928$ ,  $k_i = 0.0689$ , and  $v_0 = 0.0015$ .

To gain a quick insight into the dynamics of the proposed two DoF mechanical model (1), and to validate its accuracy on modelling the stick–slip oscillations observed in the uniform feed motion of the grinding machine, it is worthwhile to begin the numerical analysis by running time-domain simulations. Using the event-based framework introduced in Section 3, transient response signals, such as the ones shown in Fig. 6, can be generated with relative ease. Although the topologies of these displacement signals do not perfectly match the ones seen in Fig. 1, they do reliably capture the time and amplitude scales of the arising hunting motions. The starkest differences between the measured and simulated signals can be noticed in  $x_1$  while the moving column is stuck in modes 3, 6, and 9. This observation is not surprising since this is the region where accurate characterization of the friction

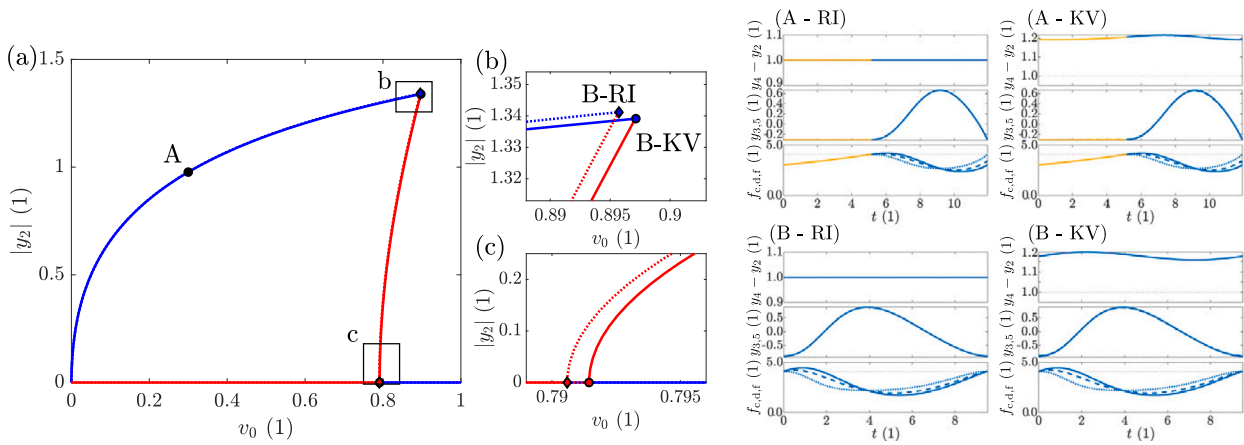


**Fig. 7.** Bifurcation map of simple limit cycle oscillations arising from the Hopf bifurcations magnified in panel (c). The solid and dotted lines denote continuation results obtained with the KV and RI contact models respectively. Blue colour marks stable solutions, while the colour red is used for unstable ones. On the panels showing time signals of the forces,  $f_c$  is marked with a solid,  $f_d$  with a dashed, and  $f_f$  with a dotted line. (The controller parameters were  $k_p = 0.732$ ,  $k_d = 1.1928$ , and  $k_i = 0.0689$ ). (For interpretation of the references to colour in this figure legend, the reader is referred to the web version of this article.)

forces is the hardest. Furthermore, in the real grinding operation there is no clear transition point between sticking and sliding friction.

#### 4.1. Continuation of periodic orbits

As demonstrated by Fig. 6, the proposed mechanical model (1) can display a wide range of intricate periodic motions, with highly different solution signatures. Therefore, to gain further insight into the dynamic behaviour of this system, it is worthwhile to use the numerical continuation techniques discussed in Section 3, to conduct bifurcation analysis on these periodic orbits found via transient simulations. It is most reasonable to begin with the simplest hunting motion illustrated in Figs. 6(a) and (c). Converted to a dimensionless form and corrected via shooting-based Newton iterations, these can be represented by the periodic orbit shown in Fig. 7 (A-RI) or (A-KV), depending on which contact model has been used.

These orbits may be continued in  $v_0$  from point A of Fig. 7, either directly via the shooting approach or by converting it to a collocation-based representation. The branches of stable periodic orbits obtained in this manner demonstrate well how the prescribed feed rate influences the dynamics of the system. In the negative  $v_0$ -direction, the branches terminate in an intersection with the equilibrium branch  $\mathbf{y}(t) \equiv \bar{\mathbf{y}}$ ,  $\mathbf{f}_1(\bar{\mathbf{y}}) = \mathbf{0}$  at  $v_0 = 0$ . Meanwhile, in the positive direction the periodic orbits encounter the grazing events ( $e_j = 7$ ) illustrated in Figs. 7(B-RI) and (B-KV), where the sticking segment spent in mode 3 disappears. Starting from these bifurcation points, following unstable smooth periodic orbits eventually leads to another pair of intersections with the equilibrium branch, where Hopf bifurcations should be expected. This can be easily verified through examining the eigenvalues of the corresponding vector field Jacobians

$$\mathbf{J}_{f_1} = \left. \frac{\partial \mathbf{f}_m(\mathbf{y})}{\partial \mathbf{y}} \right|_{\bar{\mathbf{y}}}, \quad (23)$$

where  $m = 1$ , since the equilibrium solution of the governing equation of motion is found in the first mode of the system, corresponding to stationary grinding, as illustrated by Fig. 5. Locating the exact point where  $\mathbf{J}_{f_1}$  has a pair of purely imaginary eigenvalues can also pinpoint the exact location of these subcritical Hopf bifurcations as illustrated in Fig. 7(c).

From Fig. 7 it is clear that higher feed rates lead to more desirable system dynamics, where the equilibrium solution corresponding to a constant-speed motion of the moving column that is stable. Lowering the feed rate can initially lead to a bistable configuration, where minor disturbances may cause the emergence of stable hunting motions.

Further reducing  $v_0$  also induces a loss of stability in the equilibrium solution, making constant speed motions completely infeasible.

##### 4.1.1. Rigid impact model without contact loss

Taking a closer look at Figs. 6(a) and (c) reveals that contact model selection only has a noticeable effect on the initial transient phase of the simulated time signals, as long as continuous contact is maintained between the two degrees of freedom. Fig. 7 also demonstrates, that the contact model selection has no qualitative or quantitative effect on the stability of the steady state motion or the bifurcation diagram of the system. The only noticeable difference between the found periodic orbits lies in the shape of the  $x_2 - x_1$  time signals. Therefore, while only orbits without contact loss events are examined, it is unnecessary to consider both proposed contact models separately, and one may focus solely on the one that is easier to handle numerically. Naturally, this will be the rigid impact (RI) model, which without contact-loss events reduces to a three-dimensional problem.

One of the main goals of this paper is to demonstrate the effect of controller parameter tuning on the dynamic behaviour of the grinding machine feed motion. Consequently, periodic orbit continuation was first employed to show how the bifurcation diagram presented in Fig. 7 can be influenced by the dimensionless controller parameters  $k_p$ ,  $k_i$ , and  $k_d$ .

First, the effects of the proportional gain  $k_p$  are illustrated in the bifurcation diagram in Fig. 8. Here a dashed black curve marks a set of grazing-sliding bifurcations obtained by two-parameter continuation of the orbit marked with (B-RI) in Fig. 7. This line marks the upper boundary of the bistable parameter regime in  $v_0$ , while the lower bound, which is obtained by following Hopf bifurcations of the equilibrium solution  $\mathbf{y}(t) \equiv \bar{\mathbf{y}}$ , is marked with a dashed red curve. On both ends, this former branch of grazing bifurcations terminates in a secondary grazing event corresponding to a loss of contact between the two bodies ( $e_j = 1$ ). The periodic orbits at these points are illustrated in Figs. 8(A) and (D). Following such critical contact loss orbits leads to the branches marked with dashed cyan lines. At point B the period length of these orbits approaches infinity as  $v_0$  goes to zero, while at point C a double contact loss ( $e_j = 1$  and  $e_k = 10$ ) orbit may be identified, marking an intersection between two branches of grazing contact-loss orbits with different solution signatures. Point B is important since it marks a lower bound  $k_p \approx 0.7091$ , below which branches of periodic orbits can no longer reach the equilibrium at  $v_0 = 0$ , without first encounter a contact-loss event.

The effect of the integral gain  $k_i$  is illustrated by Fig. 9. This bifurcation diagram is similar to the one shown in Fig. 8, with the important

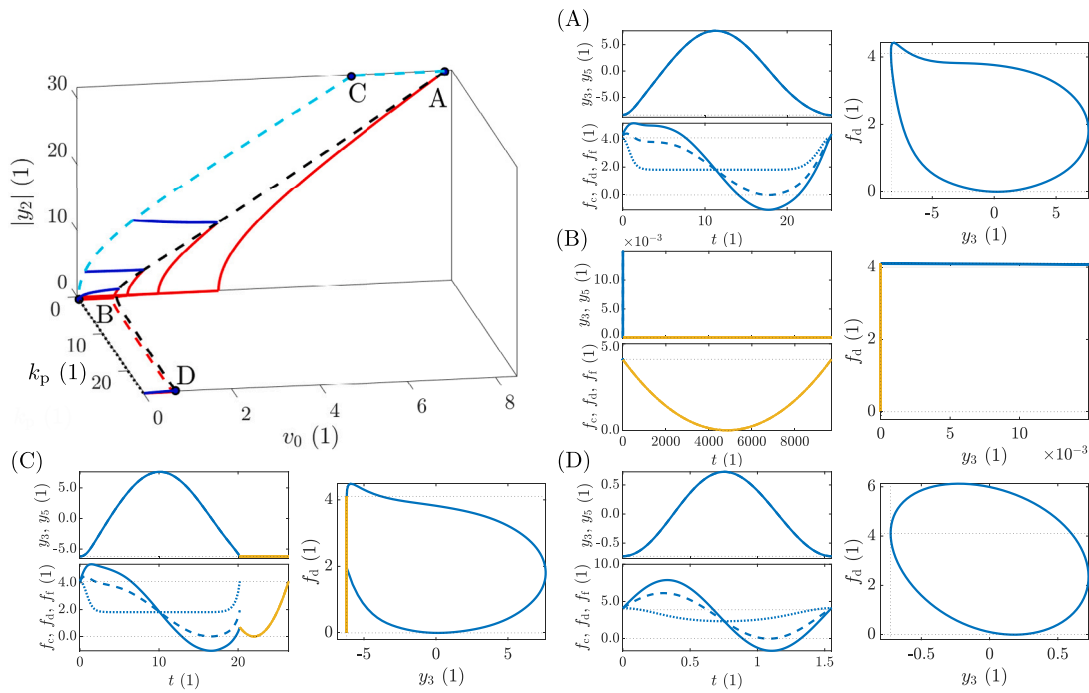


**Fig. 8.** Two parameter continuation results of the RI model in  $v_0$  and  $k_p$ . (The other two controller parameters were set to  $k_i = 0.0689$  and  $k_d = 1.928$ .) In the 3D bifurcation diagram, blue and red solid lines are used for stable and unstable branches of periodic orbits, while black, cyan, and red dashed lines mark branches of grazing-sliding, contact-loss grazing, and Hopf bifurcations respectively. In the lower left sub-panels of panels (A)–(D), solid lines are used for  $f_c$ , dashed for  $f_d$ , and dotted for  $f_r$ . (For interpretation of the references to colour in this figure legend, the reader is referred to the web version of this article.)

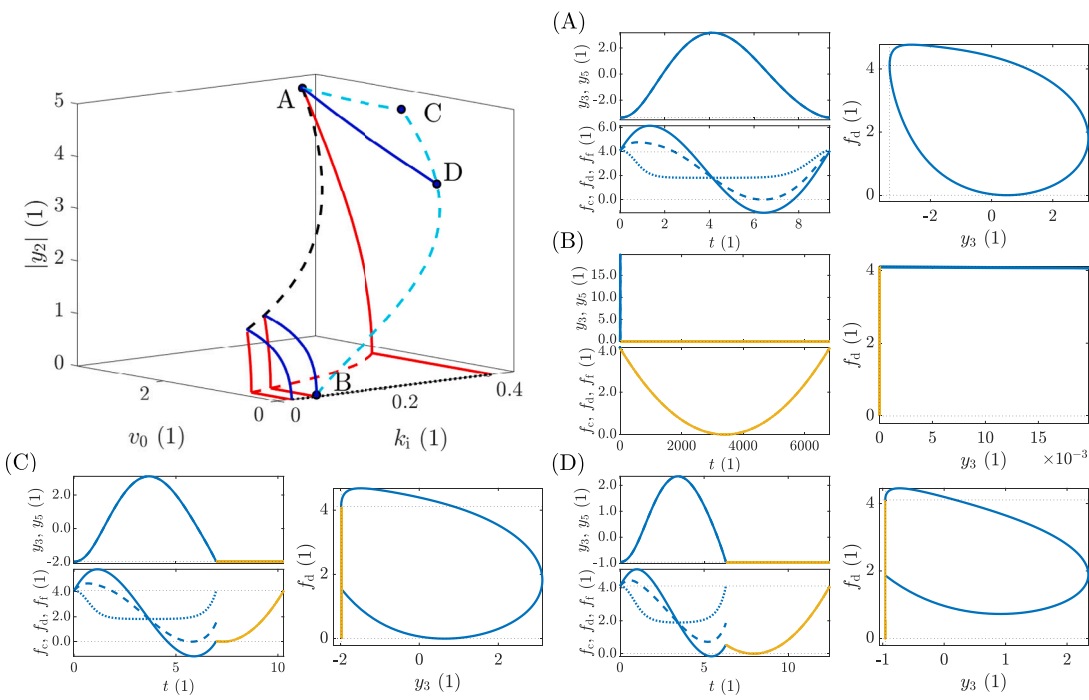


**Fig. 9.** Two parameter continuation results of the RI model in  $v_0$  and  $k_i$ . (The other two controller parameters were set to  $k_p = 0.732$  and  $k_d = 1.1928$ .) The line styles and colours are the same as in Fig. 8.

distinction that point B here marks an upper bound  $k_i \approx 0.0758$ , above which contact-loss events are to be expected. Furthermore, here only one end of the grazing-sliding bifurcation branch is marked by a contact loss event A, since there is no significant change in the periodic orbits as  $k_i \rightarrow 0$ , apart from the fact that  $y_5(t)$  grows infinitely large and cancels

out the constant part of the friction force. Fig. 8(C) shows the exact same double contact loss periodic orbit as before, while Fig. 8(D) now illustrates a standard stick–slip periodic orbit, as it encounters a grazing–sliding contact-loss event while sticking ( $e_j = 10$ ).

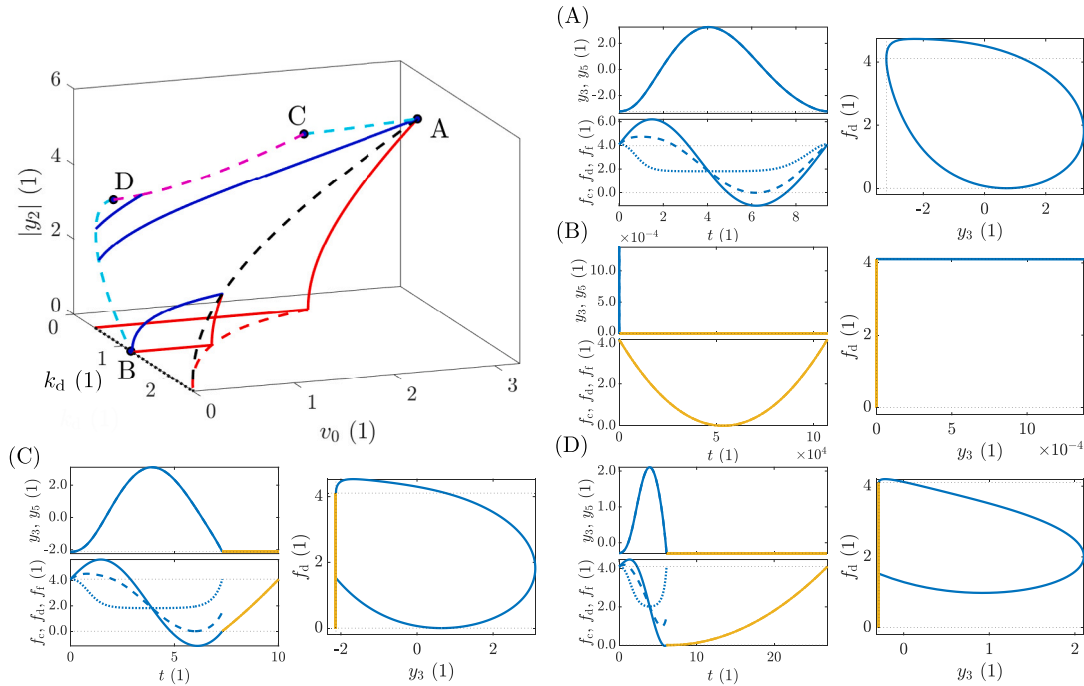


Fig. 10. Two parameter continuation results of the RI model in  $v_0$  and  $k_d$ . (The other two controller parameters were set to  $k_p = 0.732$  and  $k_i = 0.0689$ .) The use of line styles and colours is the exact same, as in the case of Fig. 8.

Finally, the influence of the derivative gain  $k_d$  is shown in Fig. 10. Here, one end of the grazing-sliding branch intersects with both the Hopf bifurcation and  $v_0 = 0$  equilibrium branches, and define an upper bound at  $k_d = 2.45$ . Above this value, the steady-state solution is stable regardless of  $v_0$  and no stick-slip oscillations are to be expected. Similarly to the previous two bifurcation diagrams, decreasing the derivative gain eventually leads to a lower limit  $k_d \approx 1.1928$ , marked by the periodic orbit shown in Fig. 10(B). Below this value the arising stick-slip oscillations become prone to contact loss events. Contrary to the previous two diagrams, the branches of critical contact-loss orbits, started from point A with grazing in  $e_j = 1$  and point B with grazing in  $e_j = 10$ , no longer intersect. This is due to the fact that they both have to be terminated prematurely due to a contact loss grazing event intersecting with the point of transition to sticking ( $e_j = 7$ ), which can also be thought of as grazing in  $e_j = 26$ . These degenerate points can be connected by a special branch of periodic orbits, which all contain a double event as illustrated by Figs. 10(C) and (D). The corresponding branch is marked by a dashed magenta curve in Fig. 10, and it connects to the cyan contact-loss branches in a smooth manner at point D and in a non-smooth manner at point C.

Overall, Figs. 8, 9, and 10 demonstrate that increasing  $k_d$  is the most straightforward solution to the problem of stick-slip oscillations since it can stabilize the equilibrium solution regardless of the prescribed feed rate. Increasing  $k_p$  and decreasing  $k_i$  may also help, albeit only to a limited degree. Decreasing  $k_d$  or  $k_p$ , or increasing  $k_i$  causes the bistable regime of  $v_0$  and the amplitude of stick-slip oscillations to grow, until eventually a contact loss event is reached.

#### 4.1.2. Rigid impact model with contact loss

After the first contact loss event is encountered, the complexity of the system dynamics blows up very quickly. Beyond the branches of grazing contact-loss orbits shown in Figs. 8–10 a wide range of periodic solutions with distinct solution signatures may be identified. Through continuing another set of grazing bifurcations corresponding to critical periodic orbits, where contact on the other side of the backlash element

is just about to be established, another important parameter boundary may be found. As illustrated in Fig. 11, such a set of grazing bifurcation branches can separate the  $v_0 - k_d$  parameter space into two regimes, one with and one without double-sided contact. In this figure, all solid curves mark branches of periodic orbits containing a contact establishing grazing event. Different colours are used to distinguish between branches with different orbit topologies and solution signatures.

To uncover this web of solution branches, first, a double-contact periodic orbit was initialized via transient simulation near point B of Fig. 10. Then it was continued in  $k_d$  up to the point where the time spent in negative contact is zero. Here a contact-establishing grazing orbit is located and then continued in both  $v_0$  and  $k_d$  until point A, where a simultaneous contact loss and transition to sticking event is encountered. At this non-smooth fold point, converting to a slightly simpler periodic orbit with one less smooth segment, enabled resuming the continuation run. The branch obtained in this manner, however, has to be terminated at point B in an identical double event ( $e_j = 26$ ). Here there is an intersection with a branch of much simpler contact establishing periodic orbits, which only contain two smooth segments. Concatenating two of these simpler orbits would result in a solution similar to the one shown in Fig. 11(B), with the minor difference, that in this case both transitions to sticking would coincide with a simultaneous loss of contact as well. This non-smooth period doubling bifurcation also connects to another branch with the same solution signature as the orbit shown in Fig. 11(B). The other end of this branch, point C, marks the disappearance of the sticking segment spent in mode 3. Here is an intersection with another branch of simple two-segment contact-establishing orbits, which here no longer implies period-doubling.

Near point C, a new branch of periodic orbits may be initialized via transient simulations, where contact loss happens without first transitioning to sticking, which means a transition directly from mode 1 to mode 4 ( $e_j = 1$ ). Continuing this branch quickly becomes highly tedious as the time spent in mode 1 increases. As illustrated by the orbits in Figs. 11(F) and (H), with each new oscillation appearing in this

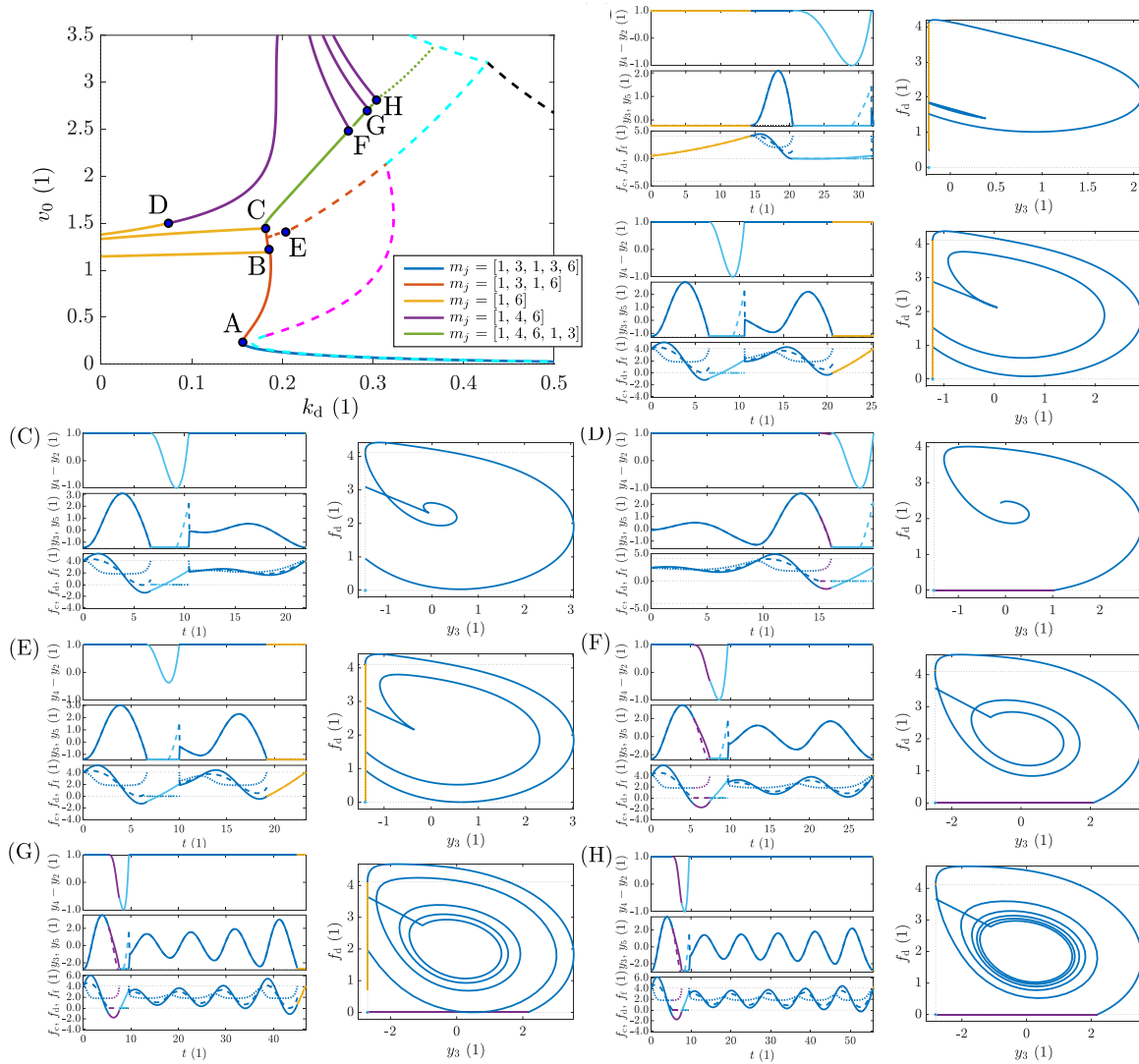


**Fig. 11.** Two parameter continuation of contact establishing grazing bifurcations in  $v_0$  and  $k_d$  considering the RI contact model. (The other two controller parameters were set to  $k_p = 0.732$  and  $k_i = 0.0689$ .) The use of line styles and colours in panels (A–H) is the exact same, as in the case of Fig. 8, with the inclusion of a new purple and cyan colour for the representation of modes 4 and 6 respectively. (For interpretation of the references to colour in this figure legend, the reader is referred to the web version of this article.)

mode, the disappearance of a sticking segment and the appearance of a new one both have to be accounted for. As an additional ripple appears in the velocity signal of the moving column a transition to sticking disappears and a new point is found where  $y_3 + v_0$  becomes zero. The analysis of this region is also further complicated by the appearance of new contact loss events, and abrupt order changes in the solution signature. From here, an example double-contact loss orbit ( $e_{j,k} = 1$ ) is shown in Fig. 11(G).

Naturally, these frequent changes in the solution signature can be handled by the shooting-based continuation scheme proposed in Section 3. However, this approach, and relying on automatic event detection, proved to be ill suited for handling contact establishing grazing bifurcations. Close to the grazing point, even vanishing disturbances caused significant deviations in the simulated orbit topologies, and thus resulted in very poor convergence. Therefore, the branches shown in Fig. 11 were all obtained via a collocation-based continuation scheme detailed in [45]. Furthermore, due to the tediousness of the manual branch switching demanded by this collocation approach, the final segment of this double contact boundary, marked with a dotted green

line in Fig. 11, is only an approximation, obtained via a brute force simulation based bisection method. This line terminates at a branch originated from point A in Fig. 10, which consists of critical contact loss grazing orbits that never leave mode 1.

Along this set of branches, whenever a new sticking segment appears, or an old one disappears, a simpler contact establishing grazing branch may be initialized where no time is spent in mode 3. Just like the branches originating from point B and C marked by yellow curves in Fig. 11, these do not directly take part in forming the double-contact parameter boundary. Nevertheless, they do separate regimes with periodic solutions of different topologies. Furthermore, even a transition point between these two types of contact establishing grazing orbits may be found. At the critical orbit illustrated by Fig. 11(D), contact is prematurely re-established in mode 6 ( $e_j = 11$ ). This event terminates the more complicated branch, and connects it to the simpler one, where the segment spent in mode 4 is no longer present, and contact loss and sticking happens simultaneously.

Finally, it is interesting to show how the contact-loss branch terminated in point C in Fig. 10 may be continued, if modes above 3 are also

considered. Allowing a direct transition to mode 6 at the encountered double event ( $e_j = 26$ ) enables further continuation of this branch up to a secondary contact loss event at point E. If the double event branch in the  $v_0 - k_d$  bifurcation diagram was not present, this would be the point equivalent to C from Figs. 8 and 9. Here, switching to a different branch of periodic orbits, with the same solution signature, also allows for a connection with the double-contact parameter boundary. This intersection, located between points B and C in Fig. 11, marks a double-grazing bifurcation point. Here a critical periodic orbit with two simultaneous grazing events can be found. One of these is the actively continued original grazing at the double event ( $e_j = 26$ ), and the other one is a newly found intersection with the negative contact-event surface in mode 6 ( $e_j = 24$ ).

#### 4.1.3. Kelvin–Voigt contact model

As demonstrated in the bifurcation diagram shown in Fig. 7, there is no noticeable difference between the RI and KV contact models as long as there is a continuous and uninterrupted contact between the elements of the feed drive assembly. Nevertheless, after the first contact loss event, the dynamic behaviour of the system is significantly influenced by the choice of contact model. Therefore, it is worth examining how the bifurcation diagrams of this system are affected by switching over to the KV model. Unfortunately, due to timescale issues, and unavoidable chatter sequences, the numeric treatment of the KV model is a lot more tedious and difficult than that of the RI model. The depth of the corresponding bifurcation analysis presented in this paper is thus not as deep, and serves as more of an extension to the results presented in the previous two subsections.

Fig. 12 presents a comparison between  $v_0 - k_d$  bifurcation maps obtainable via these two different contact models. Here the dashed lines are copied directly from Fig. 10, while the solid lines mark continuation results considering the KV contact model. Taking a closer look at the grazing sliding branches marked with black, it becomes clear that contact loss happens a lot later when the compliant contact model is employed. This is unsurprising, as contrary to  $f_{RI,d}$  from (11), the KV contact force  $f_{KV,d}$  from (10), is allowed to be negative in mode 1. This is also well demonstrated by the critical contact loss grazing orbit presented in Fig. 12(A). Here, before the grazing incidence, there is a segment where the contact force  $f_d$  is already negative, yet there is no separation in the backlash element.

Starting from point A, a branch of contact loss grazing orbits may be continued, until point B where a double contact-loss event is encountered. Here, contrary to the RI case, there is no encounter with a simultaneous transition to sticking and loss of contact ( $e_j = 26$ ), which would prematurely terminate the continuation run. If the KV contact model is considered, such a double event may only happen at specific codimension-one bifurcation points. As a result, this B point will be equivalent with the branch intersections marked by C in Figs. 8 and 9. Here, converting to a new branch of periodic orbits with contact loss grazing events in mode 3 ( $e_j = 10$ ), enables further continuation of the  $v_0 - k_d$  contact loss boundary. The new branch obtained in this manner eventually becomes close to identical to its RI counterpart, as the period length of the orbits eventually grows to infinity as  $v_0$  goes to zero. This limit is illustrated by the periodic orbit shown in Figure Fig. 12(C).

Similarly to the double contact boundary presented in Fig. 11, there is also a set of contact establishing grazing branches when the KV contact model is considered. In the exact same manner, these separate the  $v_0 - k_d$  parameter domain into regimes with and without double sided contact. Unfortunately, uncovering this boundary via numerical continuation is a lot more difficult than previously. As illustrated by the critical contact establishing grazing orbit in Fig. 12(D), the interpolation of the contact force is plagued by noticeable oscillatory numeric artefacts, when a collocation based continuation scheme is employed. These are caused primarily by the sudden and drastic peak found in  $f_d$ , right after the instant when positive contact is re-established ( $e_j = 11$ ). Consequently, even if tracking these grazing bifurcations is technically

feasible numerically, the discrete solution of the system of non-linear equations obtained via collocation, will differ significantly from the actual solution of the original PWS-ODE.

The shooting-based continuation scheme discussed in Section 3 does not suffer from these numerical interpolation artefacts, however, it is ill-suited for tracking such contact establishing grazing bifurcations. In the case of this numerical technique, an adaptive stiff differential equation solver can effectively handle the drastically different timescales of the local and global dynamics, and can capture the peak of  $f_d$  accurately. Here the problem lies in identifying a grazing point, as in the close vicinity of this bifurcation, usually multiple types of periodic orbits with different solution signatures coexist. Automatic event detection can help avoiding physically unrealistic solutions, but it also makes identifying grazing points close to impossible, as constant changes in the solution signature between subsequent solver iteration steps lead to very poor convergence. This process is only further hindered by the emergence of chatter sequences close to the contact establishing grazing incidence. Here, these quick series of contact mode changes proved to be unavoidable, no matter how the contact damping  $b_c$  was selected. Sacrificing physical meaning for the sake of better convergence, and restricting the employed shooting method to orbits with a fixed solution signature, also turned out to be ineffective. Since both the contact force  $f_{KV,d}$  from (10) and the friction force  $f_f$  from (9) are very sensitive to sign changes in their corresponding mode switching surfaces, missed non-smooth events usually lead to completely divergent solutions.

In the end, the double-contact boundary marked with dotted black curves in Fig. 12 have been obtained via the same bisection method as the dotted top part of its RI contact model counterpart shown in Fig. 11. This was done by breaking up the boundary into a lower, right, and upper part. For the upper and lower bounds, using a predefined set of  $k_d$  values, bisection searches have been conducted to find the corresponding critical  $v_0$  values. In case of the right boundary, the role of these two parameters have been reversed. The bisection searches relied on the event detection based simulation routines discussed in Section 3, and distinguished between solutions with and without double-sided contact, based on whether modes 7, 8, or 9 could be found in the modelist output by the solver, after an initial transient segment had been discarded.

#### 4.2. Controller enhancement

As demonstrated in Figs. 8, 9, and 10 with the current controller setup, the only way to completely get rid of undesirable stick-slip oscillations in the grinding machine feed drive assembly, is to significantly increase  $k_d$ . This solution, however, may lead to poor transient controller performance, and sometimes not even be feasible due to actuator power constraints. In such cases, it is worthwhile to look for other controller solutions or enhancements, even if the stability of the uniform feed motion cannot be guaranteed, since they can reduce both the timescale and amplitude of the emerging limit-cycle oscillations.

Without implementing any major modifications in the built-in industry standard controller, or conducting resource-intensive parameter tuning, the most straightforward way to improve controller behaviour is through interfering with the internal integrator state. For example, by defining a set of reset rules, where the integrator state is set to a predefined optimal value at certain times, that allows for a considerable reduction of the length of the sticking intervals. Inspired by the automata solution proposed in [41] for preventing hunting motions in set-point control applications in the presence of Stribeck-type friction, here a similar integrator reset rule has been implemented. Since the reset rule can be modelled simply by an additional non-smooth event it is straightforward to incorporate both in the dynamic model detailed in Section 2 and the numerical methods discussed in Section 3.

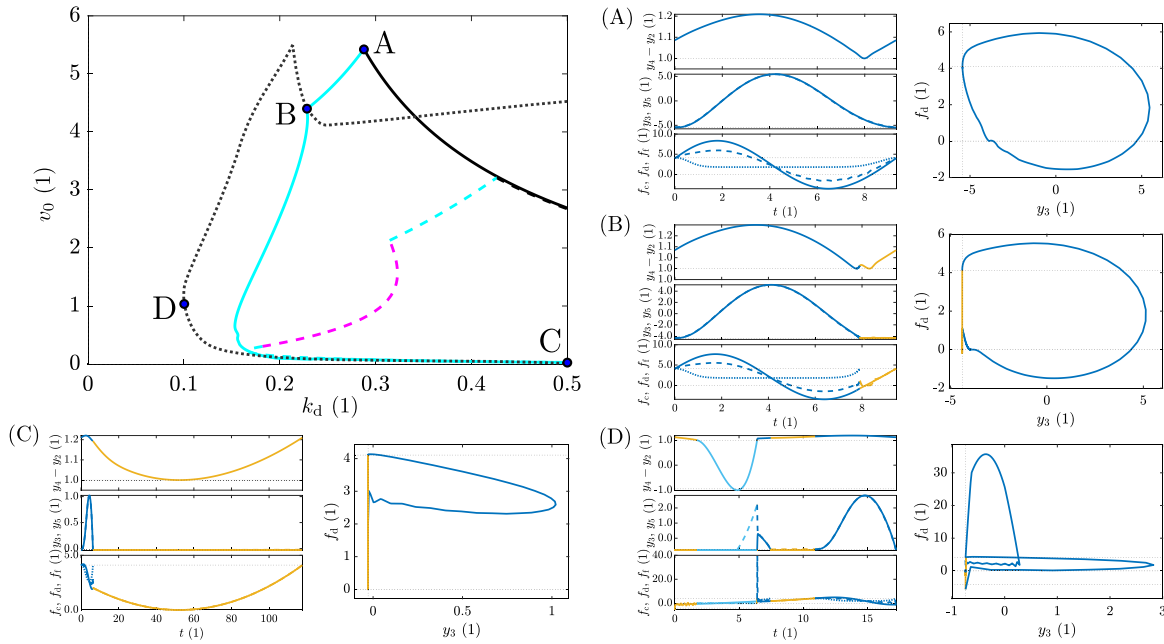


**Fig. 12.** Two parameter continuation results of the KV model in  $v_0$  and  $k_d$ . (The other two controller parameters were set to  $k_p = 0.732$  and  $k_i = 0.0689$ .) The use of line styles and colours in panels (A–D) is the exact same, as in the case of Fig. 8., with a new cyan colour added to mark time spent in mode 6 on panel (D). (For interpretation of the references to colour in this figure legend, the reader is referred to the web version of this article.)

The main goal of this controller enhancement was to reduce the period length and amplitude of the arising stick–slip oscillations indirectly, by minimizing the time spent in sticking, primarily in mode 3. To do so, the nonsmooth event

$$h_{\text{eres}}(\mathbf{y}) = y_2, \quad \mathbf{g}_{\text{eres}}(\mathbf{y}) = \begin{bmatrix} -\frac{\eta\phi+k_d y_3}{k_i} & y_2 & y_3 & y_4 & y_5 \end{bmatrix}^T, \quad \pi_{\text{eres}} = 3 \rightarrow 1, \quad (24)$$

has been appended to the governing PWS-ODE of the grinding feed drive assembly. This reset rule makes sure that the moving column separates from sticking, with just enough force to overcome the static friction, meaning  $f_c = \eta\phi$ , exactly when the position error  $y_2(t) = x_1(t)$  crosses through zero. With the new enhanced controller setup, apart from drastic cases, the position error  $x_1(t)$  should remain strictly positive, while a low level of overshoot is maintained.

The positive effects of this reset enhanced controller setup are illustrated in Fig. 13. In Fig. 13(c) a transient simulation result is displayed, with the same parameter set as the one used for producing Figs. 6(b) and (d). A comparison between these time signals demonstrates clearly, how the inclusion of this simple reset rule can drastically help reduce both the timescale and amplitude of the arising stick–slip oscillations. In Fig. 13(c), the top right graph demonstrates that, considering the timescale of an actual grinding operation, the feed rate provided by the new controller is close to uniform, and should thus be generally acceptable. The bottom right panel can also help visualize how the enhanced controller force  $f_c$  evolves in time, and how separation from sticking is induced artificially via the event map  $\mathbf{g}_{\text{eres}}$ , introduced in (24).

As illustrated in Fig. 13(c), the inclusion of an integrator reset is also capable of preventing contact loss in the considered backlash element, leading to a much smoother operation. To demonstrate the extent of this improvement, time-domain simulation based dynamic behaviour maps have been produced on the  $v_0 - k_d$  parameter domain, for both the RI and KV contact models. These rely on the solver output classification procedure discussed at the end of Section 4.1.3, but use an extensive brute-force approach on a uniformly distributed grid, instead of a

bisection based limit search. The maps acquired in this manner are shown in Fig. 13(a) and (b). Here the coloured areas separated by solid curves are obtained with the original controller, while the dotted curves show how these limits are affected by the introduction of the new nonsmooth event from (24). In these figures, the colour blue marks stable uniform feed solutions, the green area denotes periodic steady-state behaviours with stick–slip but no loss of contact, and finally the grey and white areas mark parameter regimes with contact loss and double sided contact respectively. Comparing the solid and dotted curves, it becomes clear that while the local stability of the uniform feed solution is unaffected by the new reset rule, both the first loss and first establishment of contact, on the other side of the backlash element, can be delayed via this integrator reset based controller enhancement.

In summary, extending the on-board controller with the reset rule in (24), considerably improves the dynamic behaviour of the grinding machine feed drive assembly. Although this enhancement has no effect on the local stability of the equilibrium solution and cannot prevent stick–slip oscillations, in many cases it can keep the amplitude of the arising stick–slip oscillations on an acceptable level. Furthermore, it can also considerably reduce the risk of contact loss in the considered backlash element.

### 4.3. Alternative controller setup

The controller architecture presented in Fig. 3(c) makes use of velocity and position measurements on the load side ( $x_1$  and  $\dot{x}_1$ ) of the grinding machine feed drive assembly. As mentioned previously when  $F_c$  was introduced, the velocity signals obtained in this manner, e.g. via approximate differentiation of the linear encoder position data, can at times be too noisy for precise control applications. Thus an alternative controller setup may be better suited for industrial applications, where in Fig. 3(c)  $\dot{x}_1$  is replaced by  $\ddot{x}_2$ . This leads to a new form of the controller force, where instead of (2),  $F_c$  is found using

$$F_c = -K_v \left( \ddot{x}_2 + \frac{1}{T_i} \dot{x}_2 + K_p x_1 + \frac{K_p}{T_i} \int_0^t x_1(s) ds \right), \quad (25)$$

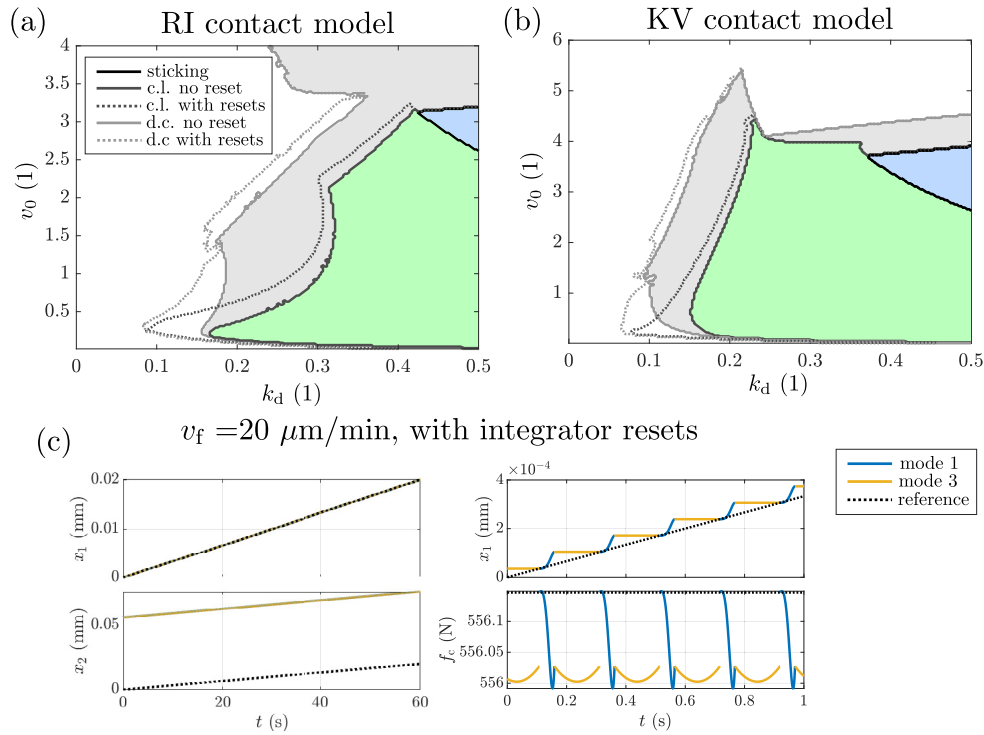


**Fig. 13.** The effect of integral resets on the dynamic behaviour of the feed drive assembly. Panels (a) and (b) display dynamic behaviour maps obtained via extensive time-domain simulations, while panel (c) illustrates how the amplitude of the stick-slip oscillations observed in Fig. 6 (b) or (d) may be reduced through integral resets.

while its dimensionless form is available as

$$f_c = -k_i y_1 - k_{p1} y_2 - k_{p2} y_4 - k_d y_5. \quad (26)$$

Here, the controller parameters  $k_d$  and  $k_i$  are equivalent to their counterparts found in (8), while  $k_{p1} = \frac{K_v K_p d^2}{m_1 v_s^2}$  and  $k_{p2} = \frac{(K_v/T_i)d^2}{m_1 v_s^2}$ .

Considering the RI contact model, in modes 1, 2, and 3 from Fig. 5, the two possible definitions of  $f_c$  from (8) and (26), apart from a shift in the steady state of the integrator term  $y_1$ , are fully equivalent. This is due to the fact, that while contact is maintained  $y_4 \equiv y_2 + 1$  and  $y_3 \equiv y_5$ , additionally  $k_p = k_{p1} + k_{p2}$ . Consequently, all results presented in Figs. 7–10 also hold for this alternative definition of the control force. Furthermore, as illustrated by Fig. 7, near the desired steady state solution of the governing equation of motion, the two considered contact models produce almost identical dynamics, and the deviations between  $y_3$  and  $y_5$  as well as  $y_2$  and  $y_4$  are negligible in the KV case as well. Thus changing the definition of  $f_c$  only has minor effects on the system dynamics in modes 1, 2, and 3, regardless of which contact model is selected. As it is designed primarily for modes 1 and 3, the integrator reset rule introduced in (24) also translates well to the alternative definition of  $f_c$ , with only minor modifications. Regardless of the type of velocity feedback, its implementation should lead to similar improvements as illustrated in Fig. 13(c).

In more drastic cases, when contact loss is expected in the considered backlash element, changing the definition of  $f_c$  to the one found in (26) may lead to significant changes in the dynamic behaviour of the feed drive assembly. Consequently the bifurcation diagrams presented in Figs. 11 and 12 may not be representative of the system dynamics. However, from an industrial point of view, trajectories and periodic solutions, which include contact loss events, are generally undesirable and of no particular importance. Thus it is simpler, yet just as powerful

to use the equivalent PID definition (8) of the built in cascaded P-PI control architecture, for parameter tuning and stick-slip prevention.

## 5. Conclusions

To help us better understand how and why stick-slip oscillations continue to plague extremely low feed rate grinding operations, even if state-of-the-art components and controller solutions are employed, a detailed numerical study has been conducted on a simplified mechanical model of a grinding machine feed drive assembly. The considered two degree of freedom model has been formulated to reproduce displacement signals obtained on an actual grinding machine, while keeping simplicity and ease of numerical treatment in mind. The resulting piecewise-smooth model included the effects of both dry friction, with a velocity weakening Stribeck effect, and actuator chain backlash. To model contact dynamics in the backlash element, completely inelastic rigid-body impacts, and a Kelvin–Voigt type nonlinear contact stiffness model have been considered.

Numerical analysis of the governing equation of motion made use of event driven transient simulations, a shooting method developed for piecewise-smooth periodic orbits built on top of this simulation engine, and a spectral collocation based continuation scheme originally developed for PWS-DDEs. Numerical continuation of periodic orbits has been employed, primarily to study the influence of the prescribed feed rate and the parameters of the built in P-PI controller. Major focus has been attributed to the identification and tracking of grazing bifurcations related to the first emergence of stick-slip oscillations, first loss of contact between the two considered degrees of freedom, and first establishment of contact on the other side of the backlash element. Where continuing periodic orbits became too tedious, due

to frequent solution signature changes or accumulating discretization errors, the formulation of bifurcation diagrams was aided by direct transient simulation based classification of system responses.

Numerical analysis demonstrated that while contact is uninterrupted, the choice of contact model is almost completely arbitrary from a dynamic behaviour point of view. When compared to experimentally obtained displacement signals, the Kelvin–Voigt model appears to be closer to reality, however, the two extra contact-dynamic parameters required are difficult to measure and highly uncertain. Considering the Kelvin–Voigt model, both the first loss of contact and the first establishment of double sided contact happened on higher oscillation amplitudes. The contact loss and contact establishing boundaries obtained with the two models had similar topologies, but the periodic orbits found considering the rigid-impact model had more complicated solution signatures. This higher level of complexity is a result of the more intricate mode transitions induced by the considered impact map. Nevertheless, when it comes to numerical treatment the compliant contact model proved to be a lot harder to handle, especially when employing collocation-based numerical techniques. This is mainly due to the drastically different timescales of the local contact and global stick–slip dynamics, which inevitably lead to significant discretization errors. Employing shooting-based continuation and stiff differential equation solvers helped in circumventing this issue. However, this approach proved to be ill-suited for tracking grazing bifurcations, due to solution signatures constantly changing between solver iteration steps, and the unavoidable emergence of chatter sequences, regardless of how the value of the contact damping was selected.

When it comes to parameter tuning of the built in cascaded P-PI controller, it has been demonstrated that the most effective approach for preventing stick–slip oscillations is to increase the derivative gain of the corresponding equivalent PID controller, as long as other limitations, such as actuator power constraints, allow for it. In this manner, the amplitude of the arising limit cycle oscillations can be reduced to zero, while the uniform feed rate equilibrium solution may also be stabilized. Decreasing the integral and increasing the proportional gain of the equivalent PID controller can also help reduce the severity of stick–slip oscillations, however, only up to a limited degree. Based on the presented numerical results, these guidelines appear powerful in preventing and mitigating stick–slip oscillations, however, prior to their implementation in an industrial setting, experimental verification is indispensable.

For more complicated cases, where increasing the equivalent derivative gain is not feasible or leads to poor transient performance, an integral state reset based controller enhancement has also been proposed. This solution is convenient as it is straightforward to implement without any major modifications to the built in controller architecture of the grinding machine. This approach introduces a reset rule, which sets the controller force equal to the static friction force just as the position error crosses through zero while the moving column of the grinding machine is sticking to its linear guides. As this leads to an immediate transition to sliding, the time spent sticking is considerably reduced. It has been shown through extensive numerical simulations that although this approach has no effect on the local stability of the desired equilibrium solution, it can help considerably reduce the amplitude of arising stick–slip oscillations. This solution does rely on *a priori* knowledge of the static friction coefficient, however, that value is still a lot easier to measure than the full velocity-dependent friction characteristics, which would be necessary for more sophisticated friction compensation techniques.

Overall, the numerical bifurcation analysis presented in this paper demonstrates well how intricate the combined effect of dry friction and backlash can be on the dynamic behaviour of any mechanical system. Furthermore, both the explosion of solution signature complexity, due to the interplay of multiple event surfaces, and the numerical errors

induced by timescale differences or chatter sequences make the handling of such dynamical systems highly difficult and tedious. Nevertheless, numerical analysis of such complex systems still warrants research effort as well as the problem of stick–slip oscillations. They both remain relevant issues in industrial fine-positioning applications.

### CRedit authorship contribution statement

**Zsolt Iklodi:** Writing – review & editing, Writing – original draft, Visualization, Software, Investigation, Formal analysis. **Petri T. Piironen:** Writing – review & editing, Supervision, Methodology. **Oier Franco:** Writing – review & editing, Data curation, Conceptualization. **Xavier Beudaert:** Supervision, Project administration, Conceptualization. **Zoltan Dombovari:** Writing – review & editing, Supervision, Project administration.

### Declaration of competing interest

The authors declare that they have no known competing financial interests or personal relationships that could have appeared to influence the work reported in this paper.

### Acknowledgements

This work is supported by the grant UNKP-23-3-II-BME-150, National Excellence Program of the Hungarian Ministry for Culture and Innovation, Hungary from the source of the National Research, Development and Innovation Fund, as well as the Basque Country Business Development Agency (SPRI) ELKARTEK 2024 MECACOGNIT, Spain (KK-2024/00030) research and collaborative project. ZI would also like to acknowledge the Erasmus+ scheme that allowed him to visit PP at Chalmers University of Technology, Sweden, where the initial modelling work took place. In particular, the Division of Dynamics at the Department of Mechanics and Maritime Sciences should be mentioned for being generous hosts.

### Data availability

No data was used for the research described in the article.

### References

- [1] H. Olsson, K.J. Åström, C.C. De Wit, M. Gäfvert, P. Lischinsky, Friction models and friction compensation, *Eur. J. Control* 4 (3) (1998) 176–195.
- [2] B. Bona, M. Indri, Friction compensation in robotics: an overview, in: *Proceedings of the 44th IEEE Conference on Decision and Control, IEEE*, 2005, pp. 4360–4367.
- [3] S. Huang, W. Liang, K.K. Tan, Intelligent friction compensation: A review, *IEEE/ASME Trans. Mechatronics* 24 (4) (2019) 1763–1774.
- [4] W. Lin, J.P. Chavez, Y. Liu, Y. Yang, Y. Kuang, Stick-slip suppression and speed tuning for a drill-string system via proportional-derivative control, *Appl. Math. Model.* 82 (2020) 487–502.
- [5] R. Beerens, A. Bisoffi, L. Zaccarian, W. Heemels, H. Nijmeijer, N. van de Wouw, Reset integral control for improved settling of PID-based motion systems with friction, *Automatica* 107 (2019) 483–492.
- [6] A.-M.O. Mohamed, A. Warkentin, R. Bauer, Prediction of workpiece surface texture using circumferentially grooved grinding wheels, *Int. J. Adv. Manuf. Technol.* 89 (2017) 1149–1160.
- [7] O. Franco, M. Gil-Inchaurrea, D. Barrenetxea, X. Beudaert, Virtual vibration absorber for active forced vibration reduction, *CIRP Ann* 72 (1) (2023) 329–332.
- [8] V. Lampaert, F. Al-Bender, J. Swevers, A generalized Maxwell-slip friction model appropriate for control purposes, in: *2003 IEEE International Workshop on Workload Characterization (IEEE Cat. No. 03EX775)*, Vol. 4, IEEE, 2003, pp. 1170–1177.
- [9] B. Armstrong-Hélouvry, P. Dupont, C.C. De Wit, A survey of models, analysis tools and compensation methods for the control of machines with friction, *Automatica* 30 (7) (1994) 1083–1138.
- [10] R.H. Hensen, M. Van de Molengraft, M. Steinbuch, Friction induced hunting limit cycles: A comparison between the lugre and switch friction model, *Automatica* 39 (12) (2003) 2131–2137.

- [11] R.T. Farouki, J.R. Swett, Real-time compensation of backlash positional errors in CNC machines by localized feedrate modulation, *Int. J. Adv. Manuf. Technol.* (2022) 1–14.
- [12] S. Shi, J. Lin, X. Wang, X. Xu, Analysis of the transient backlash error in CNC machine tools with closed loops, *Int. J. Mach. Tools Manuf.* 93 (2015) 49–60.
- [13] W. Chin, E. Ott, H.E. Nusse, C. Grebogi, Grazing bifurcations in impact oscillators, *Phys. Rev. E* 50 (6) (1994) 4427.
- [14] O.P. Yadav, S.R. Balaga, N.S. Vyas, Forced vibrations of a spring-dashpot mechanism with dry friction and backlash, *Int. J. Non-Linear Mech.* 124 (2020) 103500.
- [15] L. Márton, B. Lantos, Control of mechanical systems with stiction friction and backlash, *Systems Control Lett.* 58 (2) (2009) 141–147.
- [16] R. Zhang, Z. Wang, N. Bailey, P. Keogh, Experimental assessment and feedforward control of backlash and stiction in industrial serial robots for low-speed operations, *Int. J. Comput. Integr. Manuf.* 36 (3) (2023) 393–410.
- [17] H. Yang, Z. Wang, T. Zhang, F. Du, A review on vibration analysis and control of machine tool feed drive systems, *Int. J. Adv. Manuf. Technol.* 107 (2020) 503–525.
- [18] D.J. Ewins, *Modal Testing: Theory, Practice and Application*, John Wiley & Sons, 2009.
- [19] S. Dubowsky, F. Freudenstein, Dynamic analysis of mechanical systems with clearances—part 1: formation of dynamic model, *J. Eng. Ind.* (1971).
- [20] H.M. Lankarani, P. Nikravesh, A contact force model with hysteresis damping for impact analysis of multibody systems, *J. Mech. Des.* (1990).
- [21] W. Goldsmith, *The Theory and Physical Behaviour of Colliding Solids*, Dover Publ., 1999.
- [22] D. Garagić, K. Srinivasan, Adaptive friction compensation for precision machine tool drive, *Control Eng. Pract.* 12 (11) (2004) 1451–1464.
- [23] M. Reuss, A. Dadalau, A. Verl, Friction variances of linear machine tool axes, *Procedia CIRP* 4 (2012) 115–119.
- [24] C.-Y. Lee, S.-H. Hwang, E. Nam, B.-K. Min, Identification of mass and sliding friction parameters of machine tool feed drive using recursive least squares method, *Int. J. Adv. Manuf. Technol.* 109 (2020) 2831–2844.
- [25] O. Franco, X. Beudaert, K. Erkorkmaz, J. Munoa, Influence of guideway friction on the cutting point receptance in machine tools, *CIRP Ann* 71 (1) (2022) 361–364.
- [26] Y. Altintas, A. Verl, C. Brecher, L. Uriarte, G. Pritschow, Machine tool feed drives, *CIRP Ann.* 60 (2) (2011) 779–796.
- [27] X. Beudaert, O. Franco, K. Erkorkmaz, M. Zatarain, Feed drive control tuning considering machine dynamics and chatter stability, *CIRP Ann* 69 (1) (2020) 345–348.
- [28] O. Franco, X. Beudaert, K. Erkorkmaz, Effect of rack and pinion feed drive control parameters on machine tool dynamics, *J. Manuf. Mater. Process.* 4 (2) (2020) 33.
- [29] M. diBernardo, C. Budd, A.R. Champneys, P. Kowalczyk, *Piecewise-Smooth Dynamical Systems: Theory and Applications*, Vol. 163, Springer Science & Business Media, 2008.
- [30] M. di Bernardo, C.J. Budd, A.R. Champneys, P. Kowalczyk, A.B. Nordmark, G.O. Tost, P.T. Piiroinen, Bifurcations in nonsmooth dynamical systems, *SIAM Rev.* 50 (4) (2008) 629–701.
- [31] I. Belykh, R. Kuske, M. Porfiri, D.J. Simpson, Beyond the bristol book: Advances and perspectives in non-smooth dynamics and applications, *Chaos* 33 (1) (2023).
- [32] B. Balaram, B. Santhosh, J. Awrejcewicz, Frequency entrainment and suppression of stick-slip vibrations in a 3 DoF discontinuous disc brake model, *J. Sound Vib.* 538 (2022) 117224.
- [33] A.S. Chong, Y. Yue, E. Pavlovskaia, M. Wiercigroch, Global dynamics of a harmonically excited oscillator with a play: Numerical studies, *Int. J. Non-Linear Mech.* 94 (2017) 98–108.
- [34] H. Tao, J. Gibert, Periodic orbits of a conservative 2-DOF vibro-impact system by piecewise continuation: bifurcations and fractals, *Nonlinear Dynam.* 95 (2019) 2963–2993.
- [35] P. Kowalczyk, P. Piiroinen, Two-parameter sliding bifurcations of periodic solutions in a dry-friction oscillator, *Physica D* 237 (8) (2008) 1053–1073.
- [36] A.B. Nordmark, P.T. Piiroinen, Simulation and stability analysis of impacting systems with complete chattering, *Nonlinear Dyn.* 58 (2009) 85–106.
- [37] C. Li, J. Fan, Z. Yang, S. Xue, On discontinuous dynamical behaviors of a 2-DOF impact oscillator with friction and a periodically forced excitation, *Mech. Mach. Theory* 135 (2019) 81–108.
- [38] R. Clewley, Hybrid models and biological model reduction with PyDSTool, *PLoS Comput. Biol.* (2012).
- [39] P. Thota, H. Dankowicz, Tc-hat (tc): a novel toolbox for the continuation of periodic trajectories in hybrid dynamical systems, *SIAM J. Appl. Dyn. Syst.* 7 (4) (2008) 1283–1322.
- [40] H. Dankowicz, F. Schilder, *Recipes for Continuation*, Society for Industrial and Applied Mathematics, Philadelphia, PA, 2013.
- [41] A. Bisoffi, R. Beerens, W. Heemels, H. Nijmeijer, N. van de Wouw, L. Zaccarian, To stick or to slip: A reset PID control perspective on positioning systems with friction, *Annu. Rev. Control* 49 (2020) 37–63.
- [42] C.T. Johnson, R.D. Lorenz, Experimental identification of friction and its compensation in precise, position controlled mechanisms, *IEEE Trans. Ind. Appl.* 28 (6) (1992) 1392–1398.
- [43] C. Li, M. Xu, W. Song, H. Zhang, A review of static and dynamic analysis of ball screw feed drives, recirculating linear guideway, and ball screw, *Int. J. Mach. Tools Manuf.* 188 (2023) 104021.
- [44] T.F. Chan, Newton-like pseudo-arclength methods for computing simple turning points, *SIAM J. Sci. Stat. Comput.* 5 (1) (1984) 135–148.
- [45] Z. Iklodi, Z. Dombovari, Bifurcation analysis of piecewise-smooth engineering systems with delays through numeric continuation of periodic orbits, *Nonlinear Dynam.* (2024) 1–30.
- [46] L.N. Trefethen, *Spectral Methods in MATLAB*, SIAM, 2000.